PHYSICAL REVIEW FLUIDS **5**, 064601 (2020)

Dynamic one-equation-based subgrid model for large-eddy simulation of stratified turbulent flows

R. Ranjan,[1,*] M. K. Venkataswamy,[2,†] and S. Menon[2,‡]
[1]*Department of Mechanical Engineering, University of Tennessee at Chattanooga 615 McCallie Avenue, Chattanooga, Tennessee 37403, USA*
[2]*School of Aerospace Engineering, Georgia Institute of Technology 270 Ferst Drive, Atlanta, Georgia 30332, USA*

(Received 19 June 2019; accepted 6 May 2020; published 3 June 2020)

In this study, the dynamic one-equation-based subgrid model for large-eddy simulation (LES) of turbulent flows is extended to account for the effects of density stratification under the Boussinesq approximation. The model utilizes an eddy viscosity closure by solving a modeled transport equation for the subgrid-scale (SGS) turbulent kinetic energy (k^{sgs}) to obtain the characteristic velocity scale. The closure of the SGS density flux is attained through an algebraic eddy diffusivity-based approach using the eddy viscosity and the turbulent Prandtl number. The transport equation for k^{sgs} gets modified due to density stratification, which leads to a coupling of the SGS stress and the SGS density flux. All the model coefficients are determined locally in a dynamic manner. The dynamic model is evaluated by simulating a fully developed turbulent flow in a periodic channel under neutral and stratified conditions at frictional Reynolds number (Re_τ) of 180, 550, and 950 and frictional Richardson number (Ri_τ) of 0, 60, 120, and 240. The LES predictions are compared with direct numerical simulation results. A comprehensive assessment is performed by examining the behavior of the model coefficients, comparison of static and dynamic approaches for the model coefficients, along with comparison with other well-established algebraic closures for the SGS stress and the SGS density flux at $\mathrm{Re}_\tau = 550$. The results show that the proposed model appropriately responds to the changes in the behavior of the flow due to stratification, at both the resolved and the SGS levels, particularly in the regions away from the wall where internal waves tend to coexist with the shear-generated turbulence. An explicit coupling of the SGS buoyancy flux with the SGS kinetic energy in the dynamic model, which is absent in the other algebraic models, allows improved accuracy in capturing the instantaneous and the statistical features of both the resolved and the SGS quantities.

DOI: 10.1103/PhysRevFluids.5.064601

I. INTRODUCTION

Stratified turbulent flows are observed in several engineering, geophysical, and environmental flow systems, and therefore, the study of such flows is of great interest [1–3]. Numerical investigation of such flows under practical conditions is challenging due to the added complexity of the effects of stratification on the dynamics of turbulence. While the study of turbulence under practical scenarios is challenging on its own due to the presence of a wide range of spatial and temporal

---

[*] reetesh-ranjan@utc.edu
[†] mvenkataswamy3@gatech.edu
[‡] suresh.menon@ae.gatech.edu

scales, the presence of stratification furthers the complexity by affecting the small-scale mixing, the large-scale circulation, the interscale interactions, and the spectral characteristics [1,4–10]. Although direct numerical simulation (DNS) presents an approach to examine these fundamental aspects of interaction of turbulence with the density fluctuations resulting from the stratification [4,6,11–13], large-eddy simulation (LES) is considered a more suitable tool for investigation of high Reynolds number (Re) engineering applications. In LES, the effects of unresolved scales on the resolved scales of motion are accounted for through subgrid-scale (SGS) closures. However, the SGS closures need to be robust and accurate to account for turbulent transport processes and the effect of stratification on such processes. The present study focuses on the development and the assessment of a dynamic one-equation SGS model for LES of high Re stably stratified turbulent flows.

The effects of density stratification on turbulent flows with a mean shear have been extensively studied in the past under homogeneous [4,5,14–19] and nonhomogeneous [9,11,13,20–22] conditions. With an increase in the level of stable stratification, which is usually expressed in terms of the Richardson number, Ri (the ratio of buoyancy and the flow shear terms), primarily the turbulent mixing along the direction of stratification reduces. In addition, several physical phenomena are observed, which differ from unstratified (neutral) turbulent flows. These include the presence of internal waves, countergradient turbulent transport of momentum and density fields at different scales, increased level of anisotropy, disruption to the energy transfer across scales, modifications to coherent structures, Ri-dependent modifications to turbulent kinetic energy production and dissipation, etc. [23,24]. Such flows can be segregated into different regimes using buoyancy Reynolds number and turbulent Froude number on a hydrodynamic phase diagram [7]. These regimes include buoyancy-affected turbulence regime, buoyancy dominated regime, and buoyancy-controlled regime. Alternatively, high Re stably stratified shear flows can also be classified into three regimes using buoyancy and shear strength parameters, which include unforced, buoyancy-dominated, and shear-dominated regimes [25]. Past studies [5,14,16,18,26–28] have assessed the effects of these parameters and have performed scaling analysis to characterize the state of the stratified turbulence in terms of, for example, the effects of buoyancy on structural and spectral features, the role of shear strength and the buoyancy on stability, etc. For a detailed description of these effects, the reader is referred to the cited references.

In the wall-bounded stably stratified turbulent flows, which is the focus of this study, both the inner and outer layers get affected due to stratification [9,11,13,20–22]. In particular, with an increase in stratification, the skin friction coefficient (C_f) and Nusselt number (Nu), tend to reduce. Furthermore, interfacial wavelike motions exist in the outer or core region of the flow, where strong countergradient turbulent momentum and density fluxes are observed, In such flows, and where the length scales are large and the shear is weak, which suppresses the turbulent transport along the direction of stratification. These effects of stratification on transport and mixing make LES-based study of such flows extremely challenging, where the SGS effects on the resolved scales of motion need to accurately account for the effects of (and lack of) stratification.

Past LES of stratified flows have used different SGS models. Some of the widely used models include the modified/extended form [29,30] of the classical Smagorinsky model [31], the modified [32] or the conventional [33] form of the dynamic Smagorinsky model (DSM) [34,35], the scale similarity model [36], the dynamic mixed model [9], the extended form [32] of the deconvolution model [37], the modified form [38–40] of the one-equation-based model [41], the extended form [10] of the stretched vortex model [42], and the extended form [43] of the variational multiscale model [44]. The classical models developed for neutral flows have been either explicitly or implicitly modified to account for the effects of stratification. For example, several of the algebraic models employ a cogradient-based approach to relate the SGS stress tensor (τ_{ij}^{sgs}) with the resolved strain-rate tensor ($\overline{S}_{ij}$) using an eddy viscosity (ν_t) through: $\tau_{ij}^{\mathrm{sgs}} - \tau_{kk}^{\mathrm{sgs}}\delta_{ij}/3 = -2\nu_t\overline{S}_{ij}$, where $\nu_t = l_s^2|S|$. Here "$\overline{(\cdot)}$" and superscript "sgs" denote the resolved and the SGS quantities, respectively, and $|S| = \sqrt{2\overline{S}_{ij}\overline{S}_{ij}}$. The mixing length l_s is typically specified to be $l_s \approx C_s\overline{\Delta}$, where $\overline{\Delta}$ is the

LES filter width and C_s is a model coefficient. Under stable stratification, l_s tend to reduce, and therefore, the extended/modified formulations account for the changes in l_s due to stratification in terms of a functional dependence on local value of Ri [10,29,30,32]. The model coefficients in such closures can be specified to be constants as in the classical Smagorinsky model, or can be determined dynamically to better account for the effects of spatial and temporal variations [34,35,45,46].

In the one-equation-based model [38,39,41,45–48], which is the focus of this study, similar to the algebraic approaches, τ_{ij}^{sgs} is still related to $\overline{S}_{ij}$ by using an eddy viscosity (ν_t). However, ν_t is obtained in terms of the SGS turbulent kinetic energy (k^{sgs}) for which an additional modeled transport equation is solved [41,45–48]. Such an approach has been utilized successfully for a wide range of neutral turbulent flows and has shown an improved performance compared to the algebraic models [46,47]. In particular, the localized dynamic kinetic energy model (LDKM) [45,46] evaluates all the model coefficients dynamically in a manner similar to the DSM [34]. The LDKM formulation was originally developed for incompressible flows, and it has also been extended for compressible flows in the past [49,50]. A similar one-equation model has also been used for stratified flows in the past, where l_s is modified to account for the effects of stratification while using static values of the model coefficients [38–40]. The specification of constant values of the model coefficients lacks generality when it comes to simulation of practical applications. This issue is addressed in this study by combining the LDKM approach with the well-established SGS closure based on the modeled transport equation for k^{sgs} and explicitly accounting for the effects of stratification.

The key objective of this study is to demonstrate the capabilities of the dynamic one-equation model, which explicitly couples the SGS buoyancy flux with the SGS kinetic energy under stratification by considering a fully developed turbulent flow in a periodic channel under neutral and stably stratified conditions. The flow is simulated at $\mathrm{Re}_\tau = 180$, 550, and 950 for different values of Ri_τ (0, 60, 120, and 240). Here Re_τ and Ri_τ (defined later) denote friction Reynolds and Richardson numbers, respectively. This particular case is considered here due to its geometrical simplicity, and the presence of a wide range of turbulence physics. For example, here, two competing mechanisms coexist, one responsible for the extraction of turbulent kinetic energy from the mean shear by the wall-normal turbulent transport, and the other due to stratification, which suppresses such motions due to conversion of kinetic energy to potential energy [9,11,13,22]. The model is assessed by examining the features of instantaneous flow and density fields and comparing the turbulence statistics with the reference DNS [13] results. Additionally, various features of the model are also examined and a comparison with the algebraic no-model and the well-established DSM [34] approaches is carried out to demonstrate similarities and differences. Finally, the results are analyzed in terms of the effect of Re_τ and Ri_τ on various quantities relevant to stratified turbulent flows.

This article is arranged as follows. Section II describes the governing equations and SGS closures. The computational approach and setup are discussed in Sec. III. A comprehensive assessment of the model is described in Sec. IV and the application to wide range of Reynolds and Richardson numbers are discussed in Sec. V to demonstrate predictive capabilities of the model. Finally, the conclusions from this study and future outlook are summarized in Sec. VI.

II. MATHEMATICAL FORMULATION

A. Governing equations

The flow is incompressible with small fluctuations in the density field, which in turn allows the use of the Boussinesq approximation. The total density field (ρ_{t}) is expressed as $\rho_{\mathrm{t}} = \rho_0 + \rho$, where ρ_0 is the reference density, and ρ is the deviation about ρ_0 with $\rho \ll \rho_0$. The deviation ρ can be further expressed as $\rho(x_1, x_2, x_3, t) = \rho_{\mathrm{b}}(x_3, t) + \rho_{\mathrm{f}}(x_1, x_2, x_3, t)$, with $\rho_{\mathrm{b}}(x_3, t) \gg \rho_{\mathrm{f}}$. Here ρ_{f} is the fluctuating density, and ρ_{b} denotes an instantaneous spatially averaged quantity where the averaging is performed along the x_1 and x_2 coordinate directions, and the density stratification is along the x_3 direction. Therefore, the total density field is given by $\rho_{\mathrm{t}}(x_1, x_2, x_3, t) =$

$\rho_0 + \rho_{\mathrm{b}}(x_3, t) + \rho_{\mathrm{f}}(x_1, x_2, x_3, t)$. It is further assumed that the density fluctuation is dependent upon only one scalar field, and therefore, no equation of state is required. In some stratified flows of interest, the density fluctuation often depends upon two scalar fields, namely, temperature and salinity fluctuation through an equation of state [51]. Although we focus here on a single scalar field dependent density fluctuation, the method developed here can be extended for multiple scalar fields and will be reported in the near future.

In LES, the spatial filtering of a field variable $\phi(\boldsymbol{x}, t)$ leads to the resolved field $\overline{\phi}(\boldsymbol{x}, t)$ and the unresolved SGS field $\phi'(\boldsymbol{x}, t)$, which are related through $\phi'(\boldsymbol{x}, t) = \phi(\boldsymbol{x}, t) - \overline{\phi}(\boldsymbol{x}, t)$. In the present study, a box filter is used with filter width $\overline{\Delta}$, which corresponds to a local volume-averaging operation in the physical space, and has a global support in the spectral space. Additionally, an implicitly filtered LES formulation is considered here, which uses the computational grid as the filter. Applying the spatial filtering operation to the incompressible Navier-Stokes equation with the Boussinesq approximation leads to the following filtered LES equations:

$$\frac{\partial \overline{u}_i}{\partial x_i} = 0, \tag{1a}$$

$$\frac{\partial \overline{u}_i}{\partial t} + \frac{\partial \overline{u}_i \overline{u}_j}{\partial x_j} = -\frac{\partial \overline{p}}{\partial x_i} + \nu \frac{\partial^2 \overline{u}_i}{\partial x_j \partial x_j} - \frac{\partial \tau_{ij}^{\mathrm{sgs}}}{\partial x_i} - \delta_{i3} \frac{\overline{\rho_{\mathrm{f}}}}{\rho_0} g, \tag{1b}$$

$$\frac{\partial \overline{\rho}}{\partial t} + \frac{\partial (\overline{\rho}\, \overline{u}_j)}{\partial x_j} = \kappa \frac{\partial^2 \overline{\rho}}{\partial x_j \partial x_j} - \frac{\partial \lambda_j^{\mathrm{sgs}}}{\partial x_j}. \tag{1c}$$

Here u_i is the velocity component, p is the deviation about the hydrostatic pressure associated with $\rho_{\mathrm{b}}(x_3, t)$, ν is the kinematic viscosity, κ is the thermal diffusivity, and $i = 1, 2, 3$ denotes Cartesian coordinate directions. The terms τ_{ij}^{sgs} and λ_j^{sgs} denote the SGS stress and density flux, respectively, and require modeling to close the LES equations give by Eq. (1). These terms are given by

$$\tau_{ij}^{\mathrm{sgs}} = \overline{u_i u_j} - \overline{u}_i \overline{u}_j, \tag{2a}$$

$$\lambda_j^{\mathrm{sgs}} = \overline{u_j \rho} - \overline{u}_j \overline{\rho}. \tag{2b}$$

B. Subgrid-scale terms

A well-established and popular approach to close the SGS stress tensor τ_{ij}^{sgs} is to use the gradient diffusion hypothesis through: $\tau_{ij}^{\mathrm{sgs}} - \frac{\tau_{kk}^{\mathrm{sgs}}}{3} \delta_{ij} = -2\nu_t \overline{S}_{ij}$. Here ν_t is the subgrid eddy viscosity, and $\overline{S}_{ij} = \frac{1}{2}(\frac{\partial \overline{u}_i}{\partial x_j} + \frac{\partial \overline{u}_j}{\partial x_i})$ is the resolved strain-rate field. A classical method to obtain ν_t is to use Smagorinsky's algebraic model [31], which relates ν_t to the magnitude of the resolved strain-rate tensor and the employed grid resolution through: $\nu_t = C_s \overline{\Delta}^2 |S|$, where $|S| = \sqrt{2\overline{S}_{ij}\overline{S}_{ij}}$ and C_s is the Smagorinsky coefficient. For isotropic turbulent flows, C_s can be considered to be constant; however, for other complex turbulent flows, the value of C_s can be obtained using a dynamic approach [34].

Alternatively, a closure of ν_t can be obtained by relating it to the SGS turbulent kinetic energy k^{sgs} through [41]

$$\nu_t = C_\nu \overline{\Delta} \sqrt{k^{\mathrm{sgs}}}, \tag{3}$$

where $k^{\mathrm{sgs}} = \frac{1}{2}(\overline{u_k u_k} - \overline{u}_k \overline{u}_k) = \frac{\tau_{kk}^{\mathrm{sgs}}}{2}$. An additional modeled transport equation is solved to determine k^{sgs} [41,45–48], and the coefficient C_ν is determined locally (in both space and time) in a dynamic manner, called the locally dynamic kinetic energy model (LDKM) [45,46].

The SGS density flux [see Eq. (2b)] is closed using a gradient diffusion hypothesis through

$$\lambda_j^{\mathrm{sgs}} = -\frac{\nu_t}{\mathrm{Pr}_t} \frac{\partial \overline{\rho}}{\partial x_j}. \tag{4}$$

Here Pr_t is the turbulent Prandtl number, which can also be determined in a dynamic manner [52].

C. Modeled transport equation for SGS kinetic energy

The transport equation for k^{sgs} can be derived by subtracting product of the filtered velocity ($\overline{u}_i$) with the filtered momentum equation given by Eq. (1)(b) from the filtered product of the velocity field (u_i) with the momentum equation:

$$\frac{\partial k^{\mathrm{sgs}}}{\partial t}=\overline{u_i\frac{\partial u_i}{\partial t}}-\overline{u}_i\frac{\partial \overline{u}_i}{\partial t}. \tag{5}$$

After performing the above operation, rearranging the equations, and using Eq. (2), the exact form of the transport equation for k^{sgs} is given by

$$\frac{\partial k^{\mathrm{sgs}}}{\partial t}+\frac{\partial}{\partial x_j}(u_j k^{\mathrm{sgs}})=-\,\tau_{ij}^{\mathrm{sgs}}\overline{S}_{ij}+\nu\frac{\partial^2 k^{\mathrm{sgs}}}{\partial x_j\partial x_j}-g\frac{\delta_{j3}\lambda_j^{\mathrm{sgs}}}{\rho_0}-\nu\left[\overline{\frac{\partial u_i}{\partial x_j}\frac{\partial u_i}{\partial x_j}}-\frac{\partial \overline{u}_i}{\partial x_j}\frac{\partial \overline{u}_i}{\partial x_j}\right]$$
$$-\frac{1}{\rho_0}\left[\overline{u_j\frac{\partial p}{\partial x_j}}-\overline{u_j}\frac{\partial \overline{p}}{\partial x_j}\right]-\frac{\partial}{\partial x_j}\left[\frac{1}{2}(\overline{u_j u_k u_k}-\overline{u}_j\overline{u_k u_k})-\left(\overline{u}_i\tau_{ij}^{\mathrm{sgs}}\right)\right]. \tag{6}$$

Now, we introduce the following quantities:

$$\epsilon^{\mathrm{sgs}}=\nu\left[\overline{\frac{\partial u_i}{\partial x_j}\frac{\partial u_i}{\partial x_j}}-\frac{\partial \overline{u}_i}{\partial x_j}\frac{\partial \overline{u}_i}{\partial x_j}\right], \tag{7}$$

$$\alpha^{\mathrm{sgs}}=-\frac{1}{\rho_0}\left[\overline{u_j\frac{\partial p}{\partial x_j}}-\overline{u_j}\frac{\partial \overline{p}}{\partial x_j}\right]-\frac{\partial}{\partial x_j}\left[\frac{1}{2}(\overline{u_j u_k u_k}-\overline{u}_j\overline{u_k u_k})-\left(\overline{u}_i\tau_{ij}^{\mathrm{sgs}}\right)\right], \tag{8}$$

respectively, for SGS dissipation and turbulent diffusion, which are closed using scaling arguments and gradient diffusion hypothesis [41], respectively. Using Eq. (4) in Eq. (6) and closures for ϵ^{sgs} and α^{sgs}, we get to the following modeled transport equation for k^{sgs}:

$$\frac{\partial k^{\mathrm{sgs}}}{\partial t}+\frac{\partial}{\partial x_j}(u_j k^{\mathrm{sgs}})=-\tau_{ij}^{\mathrm{sgs}}\overline{S}_{ij}+\frac{\partial}{\partial x_j}\left[(\nu+\nu_t)\frac{\partial k^{\mathrm{sgs}}}{\partial x_j}\right]-C_\epsilon\frac{(k^{\mathrm{sgs}})^{3/2}}{\overline{\Delta}}+g\frac{\delta_{j3}}{\rho_0}\frac{\nu_t}{\mathrm{Pr}_t}\frac{\partial \overline{\rho}}{\partial x_j}. \tag{9}$$

In the right-hand-side of Eq. (9), the first three terms denote production, molecular and turbulent diffusion, and dissipation of k^{sgs}, respectively. The last term explicitly appears due to density stratification, which leads to a coupling of k^{sgs}, and hence the SGS stress tensor τ_{ij}^{sgs}, with the SGS density flux λ_j^{sgs}. This coupling is a direct manifestation of the presence of density stratification. To obtain a closed form of the transport equation for k^{sgs}, further models are introduced for ϵ^{sgs} and α^{sgs}. In Eq. (9), C_ϵ is another model coefficient, which is also determined dynamically in a similar manner to the other model coefficient C_ν [46]. The procedure to dynamically determine all the model coefficients is described elsewhere [45,49] and is not discussed here for brevity.

As stated before in Sec. I, the present work combines the LDKM approach [45,46] with the well-established closure model based on the transport equation for k^{sgs} [38–40] using constant model coefficients and explicitly accounting for the effects of stratification. Note that there exist different formulations of the modeled transport equation for k^{sgs}, such as a constant coefficient-based equation [53], one dynamic parameter-based equation, which is used here, two dynamic parameters-based equation [48], three dynamic parameters-based equation [54], etc. However, we have considered here the form given by Eq. (9), as the one-parameter-based modeled transport equation has been used extensively in several past studies of turbulent flow without stratification [45,46,49,55,56].

D. Realizability of SGS kinetic energy

The SGS kinetic energy is required to satisfy several realizability constraints, which has been described previously for neutral flows [48]. Such realizability conditions are not feasible with the algebraic Smagorinsky [31] type closures as there is no notion of explicit SGS characteristic velocity scale. One of the key required condition for k^{sgs} is its non-negativity, i.e., $k^{\text{sgs}}(\boldsymbol{x},t) \geqslant 0$, $\forall \boldsymbol{x}$ and $\forall t$, if $k^{\text{sgs}}(\boldsymbol{x},0) \geqslant 0$. This condition is part of a more general set of conditions for SGS closures [57]. Since, τ_{ij}^{sgs} is a real symmetric tensor, it can be diagonalized with real diagonal elements denoted by τ_α^{sgs}, τ_β^{sgs}, and τ_γ^{sgs}. The realizability condition requires $\tau_\alpha^{\text{sgs}} \geqslant 0$, $\tau_\beta^{\text{sgs}} \geqslant 0$, $\tau_\gamma^{\text{sgs}} \geqslant 0$, which in turn implies that $k^{\text{sgs}} = \tau_{ii}^{\text{sgs}}/2 = (\tau_\alpha^{\text{sgs}} + \tau_\beta^{\text{sgs}} + \tau_\gamma^{\text{sgs}})/2 \geqslant 0$. Here we follow the approach described by Ghosal *et al.* [48] to show that k^{sgs} given by Eq. (9) satisfies the non-negativity condition.

Without loss of generality, it can be assumed that $k^{\text{sgs}} > 0$ at $t = 0$ and $\forall \boldsymbol{x}$. Furthermore, consider $t = t_0$ to be the time at which $k^{\text{sgs}} = 0$ at some point $\boldsymbol{x} = \boldsymbol{x}_0$ in the domain. To ensure that k^{sgs} remains bounded below by zero $\forall t$, it is sufficient to show that $\partial k^{\text{sgs}}/\partial t(\boldsymbol{x}_0, t_0) > 0$. Consider an infinitesimal spherical region centered around $\boldsymbol{x} = \boldsymbol{x}_0$ with radius r. Since $k^{\text{sgs}} = \nabla k^{\text{sgs}} = 0$ at $\boldsymbol{x} = \boldsymbol{x}_0$, therefore, inside the infinitesimally spherical region, $k^{\text{sgs}} \sim r^2$ and $\nabla k^{\text{sgs}} \sim r$. Integrating Eq. (9) over the spherical region, using Eq. (3) and dividing by r^3 yields

$$\begin{aligned}\frac{\partial k^{\text{sgs}}}{\partial t} = &-\frac{1}{r^3}\int \overline{u}_n k^{\text{sgs}}\, d\sigma + \frac{1}{r^3}\int C_\nu \overline{\Delta}\sqrt{k^{\text{sgs}}}|\overline{S}|^2\, dV - \frac{1}{r^3}\int C_\epsilon \frac{(k^{\text{sgs}})^{3/2}}{\overline{\Delta}}\, dV \\ &+ \frac{1}{r^3}\int \nu \frac{\partial k^{\text{sgs}}}{\partial n}\, d\sigma + \frac{1}{r^3}\int C_\nu \overline{\Delta}\sqrt{k^{\text{sgs}}}\frac{\partial k^{\text{sgs}}}{\partial n}\, d\sigma - \frac{1}{r^3}\int \frac{\lambda_i^{\text{sgs}} g}{\rho_0}\delta_{i3}\, dV,\end{aligned} \tag{10}$$

where $d\sigma$ and dV denote infinitesimal area and volume elements of the sphere, and $\boldsymbol{n}$ is the unit normal vector. In the above equation, the first three terms are of the order r or higher. The fourth term is an order one quantity; however, it is positive and therefore can not contribute to a decrease in k^{sgs} at $\boldsymbol{x} = \boldsymbol{x}_0$ [48]. The fifth term scales as an order r quantity. The last term in Eq. (10) due to the presence of density stratification can be rewritten using Eq. (2) as

$$-\frac{1}{r^3}\int \frac{\lambda_i^{\text{sgs}} g}{\rho_0}\delta_{i3}\, dV = \frac{g\delta_{i3}}{r^3\rho_0}\int \frac{C_\nu \overline{\Delta}\sqrt{k^{\text{sgs}}}}{\text{Pr}_t}\frac{\partial \overline{\rho}}{\partial x_i}\, dV, \tag{11}$$

which is of order r for finite values of $\partial\overline{\rho}/\partial x_i$. Here it is also assumed that C_ν, C_ϵ, and Pr_t remain finite as $k^{\text{sgs}} \to 0$. Therefore, k^{sgs} can never decrease below zero at $\boldsymbol{x} = \boldsymbol{x}_0$, thus implying its non-negativity.

III. COMPUTATIONAL APPROACH AND SETUP

In this section, first, the numerical methodology is briefly described. Afterward, details of the computational setup and the simulation parameters used for different cases are discussed.

A. Numerical methodology

The governing equations given by Eq. (1) and Eq. (9) are solved using a parallel three-dimensional flow solver. The incompressible Navier-Stokes equations are solved in the primitive variable formulation using the artificial compressibility method [46]. The flow solver has been extended in this study to account for density stratification under Boussinesq approximation, for which an additional transport equation is solved for the density field. The numerical methodology is briefly described next, and further details can be found elsewhere [46].

The spatial discretization utilizes a fourth-order-accurate finite-difference method on a generalized curvilinear nonstaggered structured grid. The semidiscrete equations obtained after the spatial discretization are advanced in time using a second-order accurate backward-difference method. The artificial compressibility method utilizes a dual time-stepping algorithm to perform pseudo-time integration of the transport equations for the pressure, momentum, density, and SGS kinetic energy fields. This is achieved by using a five-stage Runge-Kutta time-stepping scheme. The numerical method is energy conserving and hence, it can be used to perform DNS and LES of turbulent flows. The solver has been extensively used in the past to study a wide range of turbulent flows,

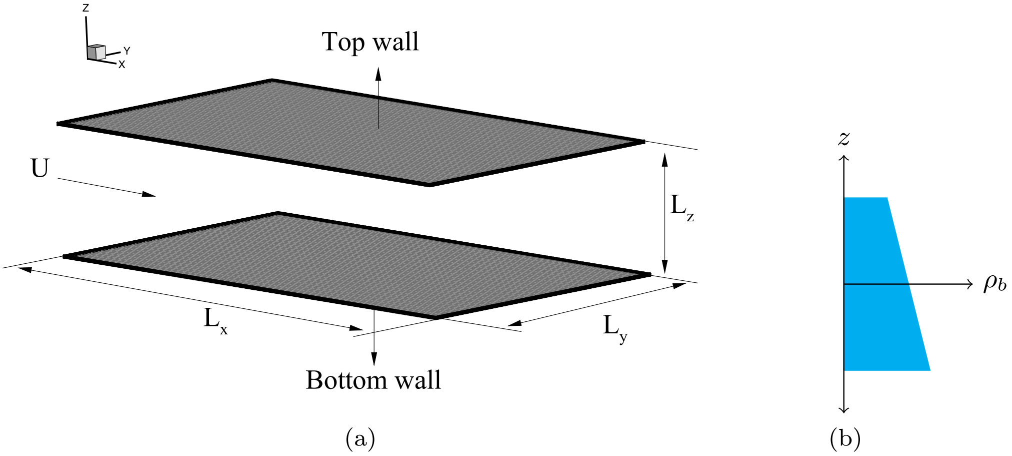

FIG. 1. Schematics of the computational domain for fully developed turbulent flow in a channel (a) and the density stratification along the vertical direction (b). In panel (b), ρ_b denotes deviation in the density field about the reference value ρ_0 along the vertical direction.

such as isotropic turbulence, channel flow, separating or reattaching flows, wakes, mixing layers, etc. [46,55,56,58,59]. The parallelization of the solver utilizes the standard domain decomposition procedure for which the message passing interface library is used.

B. Description of cases

Figure 1 shows a schematic of the computational setup, where the domain extent is chosen to be $L_x = 4\pi h$ in the streamwise (x), $L_y = 2\pi h$ in the spanwise (y), and $L_z = 2h$ in the vertical (z) directions, with h being the channel half-height. A periodic boundary condition is used along the x and y directions for all the field variables. On the bottom and top walls of the channel, a no-slip condition for the velocity field, and Dirichlet boundary condition for the density field are specified. In particular, the density field on the walls of the channel is specified as $\overline{\rho}(x, y, z = \mp h) = \pm\Delta\rho/2$, which leads to a stable stratification along the z direction when a finite value of Richardson number is used. Here $\Delta\rho$ denotes the mean density difference between the bottom and the top walls of the channel. Note that the use of such a Dirichlet type of boundary condition for the density field leads to a wall-normal density flux, which gets affected due to turbulence and stratification. Hereafter, $\boldsymbol{x} \equiv (x_1, x_2, x_3) \equiv (x, y, z)$ are used interchangeably.

The flow in the channel is driven by a constant pressure gradient so that in the statistically stationary state, a prespecified value of $\mathrm{Re}_\tau = u_\tau h/\nu$, is approximately attained. Here u_τ denotes the friction velocity. Simulations with different values of $\mathrm{Ri}_\tau = \Delta\rho g h/(\rho_0 u_\tau^2)$ are considered in this study. When $\mathrm{Ri}_\tau = 0$, the density field acts as a passive scalar, which does not affect the flow field, and for a finite value of Ri_τ, the density field acts as an active scalar, which affects both the flow and the density fields due to stratification. In unbounded shear flows, the gradient Richardson number ($\mathrm{Ri}_\mathrm{g} = N^2/S^2$) is used to characterize the effects of stratification [14,60]. Here N is the Brunt-Väisälä frequency (buoyancy frequency), and S is the mean shear rate, which for the present flow configuration are, respectively, defined as $N = \sqrt{-\frac{g}{\rho_0}\frac{d\langle\overline{\rho}\rangle}{dz}}$, and $S = d\langle\overline{u}\rangle/dz$, where $\langle\cdot\rangle$ denotes the statistical averaging operation. It is apparent that in the present flow configuration, Ri_g varies along the vertical direction, and, therefore, it is not used as a parameter to characterize the level of stratification in different cases. Linear stability analysis [60] and past experimental studies [14] have shown that $\mathrm{Ri}_g \geqslant 0.25$ is a sufficient condition for stability in stratified shear flows. As discussed later, in all the stratified cases considered here, $\mathrm{Ri}_\mathrm{g} > 0.25$ for $0.8 \lessapprox z/h < 1$ and becomes singular

TABLE I. Simulation parameters characterizing different cases considered in this study. Cases labeled as "A," "B," and "C" correspond to $\mathrm{Re}_\tau = 180$, 550, and 950, respectively, with neutral cases denoted by "A0," "B0," and "C0." For a fixed value of Re_τ, for example, $\mathrm{Re}_\tau = 550$, the increase in Ri_τ is denoted by "B0," "B1," "B2," and "B3." The superscripts "nm," "st," and "ds" for a case denote different types of SGS models, with no superscript being used for the baseline dynamic one-equation SGS model developed in this study. The subscript "f" denotes a relatively finer grid compared to the one used by the baseline neutral (Case B0) and stratified (Case B1) cases. The reference cases at $\mathrm{Re}_\tau = 180$ and 550 correspond to the past DNS study of stably stratified turbulent channel flow [13].

Case	Re_τ	Ri_τ	Ri_b	Pr_t^{-1}	$N_x \times N_y \times N_z$	$(\Delta x^+,\ \Delta y^+)$	$(\Delta z^+_\mathrm{min},\ \Delta z^+_\mathrm{max})$	$10^3 C_\mathrm{f}$	Nu
A0-DNS [13]	180	0	0	–	256 × 256 × 97	(8.8, 4.4)	(–, 5.9)	8.1	6.03
$\mathrm{A0}_\mathrm{f}$	184	0	0	Dynamic	64 × 64 × 65	(35.9, 18.0)	(0.3, 9.0)	7.73	6.4
A1-DNS [13]	180	60	0.08	–	256 × 256 × 97	(8.8, 4.4)	(–, 5.9)	5.5	2.8
$\mathrm{A1}_\mathrm{f}$	183	60	0.07	Dynamic	64 × 64 × 65	(35.9, 18.0)	(0.3, 9.0)	4.69	3.1
B0-DNS [13]	550	0	0	–	768 × 853 × 257	(9.0, 4.1)	(–, 6.7)	5.9	16.44
B0	550	0	0	Dynamic	140 × 140 × 111	(49.7, 24.9)	(0.83, 24.4)	5.84	17.5
$\mathrm{B0}^\mathrm{nm}$	559	0	0	–	140 × 140 × 111	(49.7, 24.9)	(0.83, 24.4)	6.03	18.6
$\mathrm{B0}^\mathrm{st}$	554	0	0	1	140 × 140 × 111	(49.7, 24.9)	(0.83, 24.4)	5.91	17.6
$\mathrm{B0}^\mathrm{ds}$	559	0	0	Dynamic	140 × 140 × 111	(49.7, 24.9)	(0.83, 24.4)	6.04	17.0
$\mathrm{B0}_\mathrm{f}$	550	0	0	Dynamic	192 × 192 × 192	(36.2, 18.1)	(0.48, 14.0)	5.84	17.5
B1-DNS [13]	550	60	0.07	–	768 × 853 × 257	(9.0, 4.1)	(–, 6.7)	4.8	6.95
B1	552	60	0.07	Dynamic	140 × 140 × 111	(49.7, 24.9)	(0.83, 24.4)	4.81	8.0
$\mathrm{B1}^\mathrm{nm}$	555	60	0.07	–	140 × 140 × 111	(49.7, 24.9)	(0.83, 24.4)	4.87	7.4
$\mathrm{B1}^\mathrm{st}$	556	60	0.07	1	140 × 140 × 111	(49.7, 24.9)	(0.83, 24.4)	4.89	7.8
$\mathrm{B1}^\mathrm{ds}$	564	60	0.07	Dynamic	140 × 140 × 111	(49.7, 24.9)	(0.83, 24.4)	5.03	11.8
$\mathrm{B1}_\mathrm{f}$	552	60	0.07	Dynamic	192 × 192 × 192	(36.2, 18.1)	(0.48, 14.0)	4.82	8.3
B2	555	120	0.13	Dynamic	140 × 140 × 111	(49.7, 24.9)	(0.83, 24.4)	4.37	6.5
B3	556	240	0.21	Dynamic	140 × 140 × 111	(49.7, 24.9)	(0.83, 24.4)	3.43	5.3
C0	947	0	0	Dynamic	256 × 256 × 192	(46.8, 23.4)	(0.81, 24.3)	4.58	27.4
C1	956	60	0.06	Dynamic	256 × 256 × 192	(46.8, 23.4)	(0.81, 24.3)	3.86	13.7

at the center of the channel, thus indicating higher levels of stratification in the core region and towards the center of the channel. An alternate way to characterize the level of stratification in this particular flow is to use the bulk Richardson number $\mathrm{Ri}_\mathrm{b} = \Delta\rho g h/(2\rho_0 U_\mathrm{b}^2)$, where U_b is the bulk velocity. Based on the value of Ri_b, the stratified cases considered here correspond to moderate to high levels of stratification [21].

The effects of stratification can also be characterized in terms of the global quantities such as coefficient of friction (C_f), and Nusselt number (Nu), which are defined as

$$C_\mathrm{f} = \frac{\tau_\mathrm{w}}{\frac{1}{2}\rho_0 U_\mathrm{b}^2}, \qquad \mathrm{Nu} = \frac{2hQ_\mathrm{w}}{\kappa\Delta\rho}, \tag{12}$$

where τ_w, and $Q_\mathrm{w} = -\kappa(\partial\langle\overline{\rho}\rangle/\partial z)_\mathrm{w}$ denote the wall shear stress, and wall density flux, respectively. Hereafter, the subscript "w" denotes the value of a quantity at the wall. The nondimensionalization of variables is performed using h for the length scale, u_τ for the velocity scale, and ρ_τ or $\Delta\rho$ for the density scale. Here $\rho_\tau = Q_\mathrm{w}/u_\tau$ is the friction density.

Table I summarizes the simulation parameters for all the cases considered here. Different cases are considered to (a) verify the ability of the current SGS model to capture the effects of stratification, (b) examine the role of static versus dynamic approach to specify Pr_t, (c) demonstrate the adequacy of the baseline grid resolution, (d) compare with other types of SGS closures, and (e) show the predictive capabilities for a range of values of Re_τ and Ri_τ. The cases are labeled as "A," "B," and "C" for $\mathrm{Re}_\tau = 180$, 550, and 950, respectively. The subscript "f" denotes a relatively fine grid case, and the superscripts "nm," "st," and "ds" denote the no-model (SGS terms are neglected), static, and dynamic Smagorinsky [34] approaches for the SGS closures, respectively. The cases employing static models differ from the dynamic approach only in terms of the way Pr_t is specified. In Table I the parameters for reference DNS cases [13] are also included, where the grid size is adjusted for the computational domain used in this study.

The baseline case for which a comprehensive assessment is performed corresponds to $\mathrm{Re}_\tau = 550$ and is referred to as Case B0 and Case B1 for neutral ($\mathrm{Ri}_\tau = 0$) and stratified ($\mathrm{Ri}_\tau = 60$) conditions, respectively. The grid resolution chosen for the baseline cases is typical of LES grid resolution for a wall-resolved LES [61,62], where the streamwise and spanwise resolutions are approximately chosen to be 50 and 25 wall units, respectively. The minimum near-wall resolution is approximately 1 wall unit and the maximum is about 25 wall units due to the use of a stretched grid in the vertical direction. The relatively fine grid cases use a grid matching the coarsest resolution considered in the past LES studies of stably stratified turbulent channel flows [9,11]. Note that these relatively fine grid cases are not considered to demonstrate grid convergence, rather the goal is to show that the baseline grid, where the total number of grid points is about 30% of the points in the relatively finer grid case, is adequate to capture the flow features.

The flow in the channel is initialized by imposing three-dimensional perturbations on the mean velocity profile. After the flow evolves to a statistically stationary state, the turbulence statistics are obtained by averaging along the homogeneous x and y directions and then obtaining a running average over time. Hereafter, $\langle\phi\rangle(z)$ denotes the statistically averaged value of $\phi(\boldsymbol{x}, t)$. The statistically stationary state of turbulence in the channel is ensured by monitoring the time evolution of Re_τ and Nu. All of the stratified cases are started after the corresponding neutral cases reach a statistically stationary state for computational efficiency.

IV. ASSESSMENT OF THE MODEL

We use the baseline neutral (Case B0) and the stratified (Case B1) cases corresponding to $\mathrm{Re}_\tau = 550$ to assess the modified dynamic one-equation model reported here. The analysis is performed in terms of the effects of stratification on the instantaneous behavior of the resolved and the SGS quantities. Afterward, the assessment is performed in terms of the turbulence statistics by comparing them with the available data from a past DNS study [13]. The model is further examined in terms of a comparison with the other well-established algebraic SGS models. The effects of grid resolution and the use of static versus dynamic approach for specifying Pr_t are discussed in the Appendix.

A. Effects of stratification on instantaneous flow features

The key instantaneous features of stably stratified turbulent flows include the suppression of turbulent transport of the density field along the direction of stratification and the presence of internal waves, which affect the overall dynamics of such flows [23,24]. These features are captured by the dynamic SGS model employed in this study, as evident in Fig. 2, where the contours of the normalized density field ($\rho^* = \overline{\rho}/\Delta\rho$), the isosurface of $\rho^* = 0$, and the probability density function (PDF) of the vertical location of the points corresponding to the isosurface of $\rho^* = 0$ are shown for the neutral (Case B0) and the stratified (Case B1) cases.

The isocontours of ρ^* in the central x-z plane (also referred to as isopycnals [9]), show that in Case B0 [see Fig. 2(a)], an effective turbulent transport occurs vertically, where the fluctuations tend to cross the central plane of the channel. However, in Case B1 [see Fig. 2(b)], such fluctuations tend to segregate in the top and the bottom halves of the channel, and a wavy structure appears in the core of the channel. It is apparent that the turbulent transport gets severely suppressed by the stable stratification. Additionally, the center of the channel acts as a barrier to the transport causing the formation of a sharp density interface (also referred to as a pycnocline [2]). The stratification also affects the overall scales of the motion as evident from the isosurface of $\rho^* = 0$ shown in

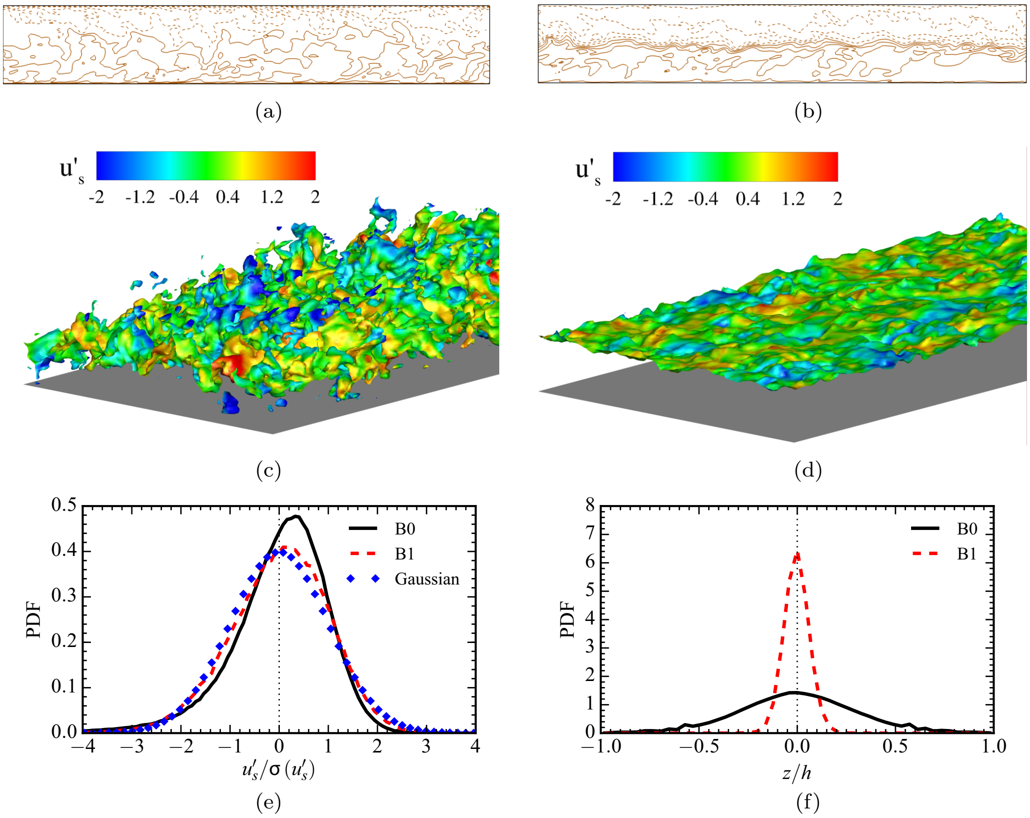

FIG. 2. Instantaneous contours of ρ^* in the central vertical plane (a), (b), isosurface of $\rho^* = 0$ colored by the contours of the normalized streamwise velocity fluctuations (c), (d), PDF of the surface ($\rho^* = 0$) streamwise velocity fluctuations (e), and PDF of the vertical location of points corresponding to the isosurface of $\rho^* = 0$ at $\mathrm{Re}_\tau = 550$ for the neutral (Case B0) and the stratified (Case B1) cases. In panels (a) and (b) positive and negative isocontours are represented by solid and dashed curves, respectively.

Figs. 2(c) and 2(d). Under a laminar flow condition, this isosurface remains a planar surface located at $z/h = 0$. Due to the effects of turbulence, and under neutral conditions, the isosurface undergoes intense wrinkling and stretching leading to the appearance of small-scale structures. However, under stable stratification, such small-scale features disappear and formation of an internal wavy structure occurs in the core of the channel.

The isosurface of ρ^* shown in Figs. 2(c) and 2(d) are colored by the normalized streamwise surface velocity fluctuation $[u'_s = (\overline{u} - \overline{u}_s)/u_\tau]$, which show a reduced level of variation of the streamwise velocity fluctuations in Case B1. This is also evident from the PDF of u'_s shown in Fig. 2(e). Here ϕ_s denotes surface-averaged value of the quantity ϕ, defined as $\phi_s(t) = \frac{1}{\mathcal{S}} \int_{\mathcal{S}} \phi(\boldsymbol{x}, t)|_{\mathcal{S}}\, d\mathcal{S}$, where $\mathcal{S}$ denotes the isosurface of $\rho^* = 0$. The PDF of u'_s exhibits a Gaussian behavior for Case B1 compared to Case B0 where the PDF exhibits a much wider tail. In particular, the skewness and the kurtosis are -1.1 and 6.2, respectively, in Case B0, compared to Case B1, where the values of these quantities are respectively, -0.4 and 3.5. These statistics show that the PDF of the vertical location of the points for Case B1 [corresponding to the isosurface of $\rho^* = 0$; see Fig. 2(f)] is much narrower than for Case B0.

The presence of internal waves and the effects of stratification on turbulence can be inferred from the phase relationship between the vertical velocity and density fluctuations [5,21,63]. The phase

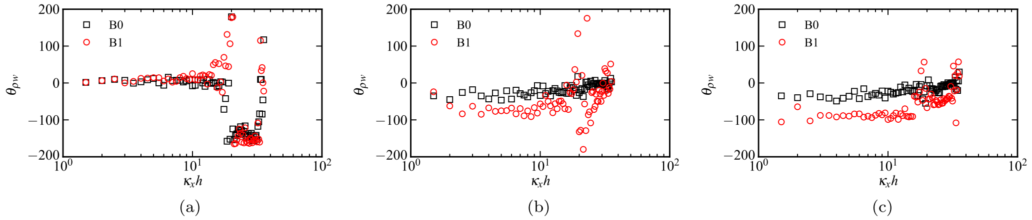

FIG. 3. Streamwise spectrum of the phase angle $\theta_{w\rho}$ for the neutral (Case B0) and the stratified (Case B1) cases at different vertical locations measured from the bottom surface. (a) $z^+ = 10$, (b) $z^+ = 450$, and (c) $z^+ = 550$.

angle is defined as $\theta_{\rho w}(\kappa_x, z, t) = \tan^{-1}[\frac{\mathrm{Qu}_{\rho w}(\kappa_x,z,t)}{\mathrm{Co}_{\rho w}(\kappa_x,z,t)}]$, where $\mathrm{Co}_{\rho w}$ and $\mathrm{Qu}_{\rho w}$ denote the cospectrum and quadrature spectrum of $\rho' w'$ and κ_x is the streamwise wave number. While $\theta_{\rho w} \approx 0$ indicates shear-driven vertical density flux, $\theta_{\rho w} \approx \pm 180^{\circ}$ implies flux reversal at corresponding scales, which can be attributed to buoyancy-driven countergradient vertical density flux. However, $\theta_{\rho w} \approx \pm 90^{\circ}$ suggests possible presence of large-scale internal waves. The streamwise spectrum of $\theta_{\rho w}$ for the neutral (Case B0) and the stratified (Case B1) at different vertical locations are shown in Fig. 3. In the near-wall region ($z^+ = 10$), in both the cases, $\theta_{\rho w} \approx 0$ at the energetic lower wave numbers and $\theta_{\rho w} \approx \pm 180^{\circ}$ at the higher wave numbers. At the locations away from the wall ($z^+ = 450$ and 550), in the stratified case, $\theta_{\rho w} \approx \pm 90^{\circ}$ for the energetic small wave numbers, thus indicating a possible presence of large-scale internal waves in these regions.

The effect of stratification in spectral space is analyzed by considering the normalized streamwise spectrum of the resolved vertical turbulent kinetic energy (E_{33}) and the density field (Φ), which are shown in Fig. 4 at different vertical locations. At all locations, both E_{33} and Φ show a presence of inertial range due to a reasonably high Re of the flow considered here. Near the wall ($z^+ = 10$), the energy spectrum in both Case B0 and Case B1 nearly overlaps, thus illustrating a negligible effect of

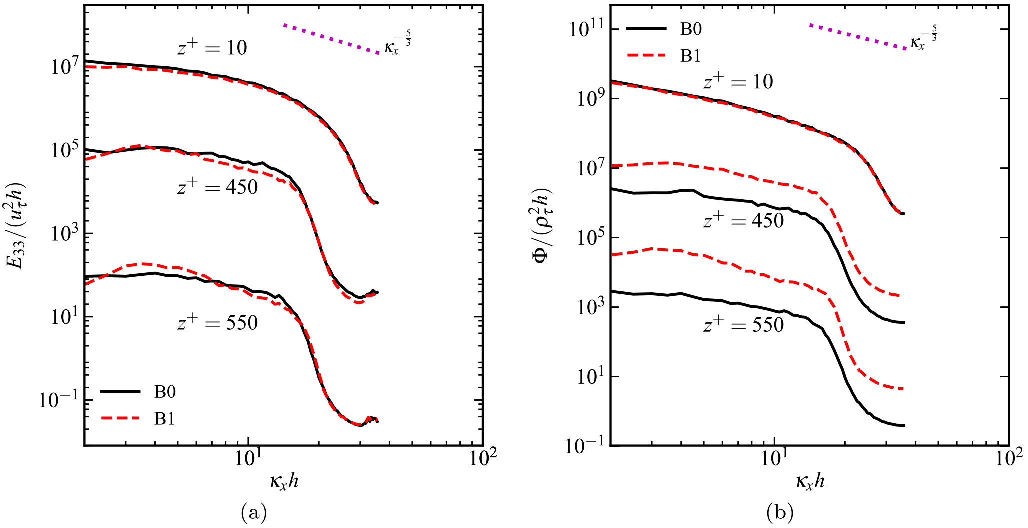

FIG. 4. Streamwise spectrum of the vertical component of the resolved turbulent kinetic energy (a) and the density field (b) at different vertical locations for the neutral (Case B0) and the stratified (Case B1) cases. A reference curve indicating $\kappa_x^{-5/3}$ is also included in both panels to show the presence of an inertial range. The spectra at locations $z^+ = 10$, 450, and 550, are scaled by a factor of 10^6, 10^3, and 1, respectively, for clarity.

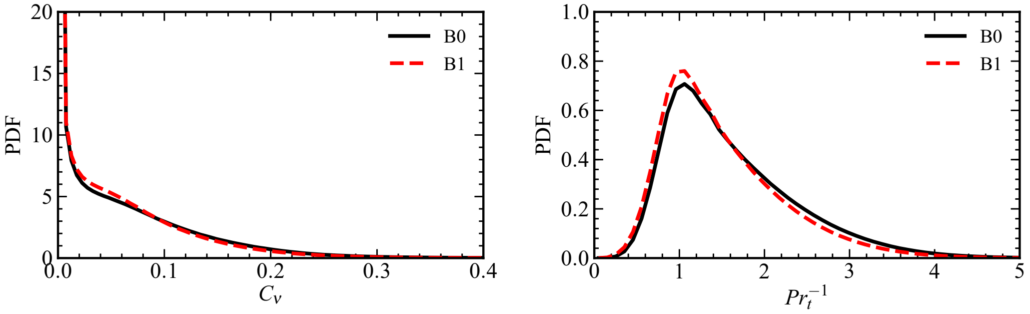

(a) (b)

FIG. 5. PDF of the model coefficients C_ν (a) and Pr_t^{-1} (b) used by the closure expressions for τ_{ij}^{sgs} and λ_j^{sgs} in Eq. (3) and Eq. (4), respectively, for the neutral (Case B0) and the stratified (Case B1) cases.

stratification. However, farther away from the wall ($z^+ = 450$ and 550), the stratification suppresses the energy corresponding to the large scales ($\kappa_x h \lessapprox 2$) by affecting the global modes generated by tall eddies (eddies of size h) that stir the mean velocity profile over the whole channel height [13]. The vertical component of kinetic energy shows an increase for a range of scales ($2 \lessapprox \kappa_x h \lessapprox 6$) in Case B1, consistent with the past observation [22]. This increase can be attributed to the effect of internal waves in the core of the channel (see Fig. 3) where although the turbulence buoyancy flux reduces due to stratification [see Fig. 11(b) below], the fluctuations in the density and the vertical velocity tend to increase [see Figs. 10(b) and 10(d) below]. Thus, the behavior of the spectra at the small scales are not affected at all the vertical locations since the stable stratification mainly affects the large scales. The kink observed in the variation of E_{33} at higher wave numbers, particularly at the wall-normal locations $z^+ = 450$ and 550, is due to numerical aliasing at the cutoff scale [10].

The normalized density spectrum in the near-wall region ($z^+ = 10$) nearly overlaps in cases B0 and B1 in a manner similar to the normalized spectrum of the resolved vertical turbulent kinetic energy. The effects of stratification is apparent at the other two locations ($z^+ = 450$ and 550), where the level of fluctuations in the density field enhances. Such a behavior in the stratified case occurs due to the presence of internal waves in the core of the channel and a very sharp gradient of the density field near the center of the channel.

The density stratification also affects the SGS model coefficients such as C_ν and Pr_t, which are used in Eq. (3), and Eq. (4), respectively. This is evident from the PDF of these quantities shown in Fig. 5, where it can be observed that although the effect of stratification on C_ν tends to be marginal, it is noticeable for Pr_t^{-1}. Quantitatively, the mean and the standard deviation of C_ν is about 0.04 and 0.07, respectively, for both the cases. However, for Pr_t^{-1}, the mean and standard deviation both reduce in Case B1 by about 7% compared to Case B0. Note that Pr_t^{-1} depends upon several factors such as Re_τ, Pr, grid resolution, etc. It has been shown in the past studies [13,52,64] that for the flow considered here, $\mathrm{Pr}_t^{-1} < 1$ can occur in the time-averaged statistics in the viscous sublayer region, which implies that $\mathrm{Pr}_t^{-1} < 1$ can be observed in the instantaneous results as evident here. However, in Fig. 5(b), the number of samples where $\mathrm{Pr}_t^{-1} < 1$ is about 22% and 26% of the total number of samples for cases B0 and B1, respectively, which leads to the time-averaged value of $\mathrm{Pr}_t^{-1} > 1$ throughout the channel (discussed later).

The SGS quantities also get affected by stratification, which occur explicitly through the last term in Eq. (9). Essentially, the vertical component of the SGS density flux (λ_3^{sgs}) explicitly affects k^{sgs} and thus ν_t, in the stratified case. This is evident from the variation of λ_3^{sgs} with respect to k^{sgs} as shown in Fig. 6 at $z^+ = 550$. The variation in the near-wall region (not shown here) remains similar in both the cases. However, away from the wall, the scatter of the normalized λ_3^{sgs} tends to increase for fixed values of the normalized k^{sgs} in the stratified case. This is further evident from the PDF of $\lambda_3^{\mathrm{sgs}}/(\rho_\tau u_\tau)$ shown in Fig. 7 for fixed values of $k^{\mathrm{sgs}}/u_\tau^2$ at $z^+ = 10$, 450, and 550. At $z^+ = 10$,

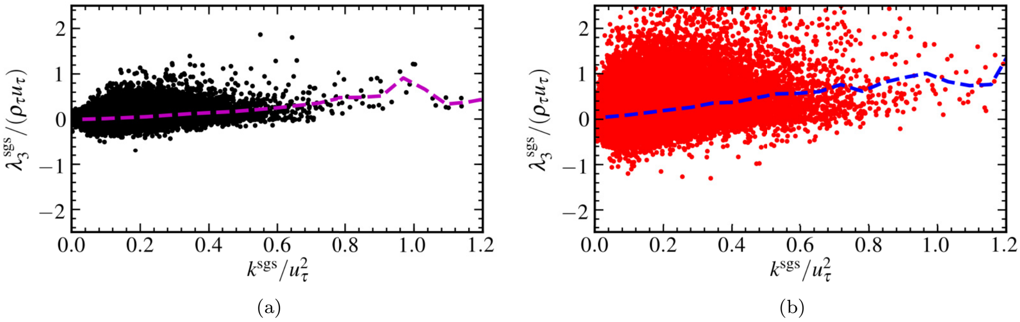

FIG. 6. Variation of vertical component of the normalized SGS density flux $[\lambda_3^{sgs}/(\rho_\tau u_\tau)]$ with respect to the normalized SGS turbulent kinetic energy (k^{sgs}/u_τ^2) for the neutral (Case B0) (a) and the stratified (Case B1) (b) cases. Dashed curve denotes the conditional average of $\lambda_3^{sgs}/(\rho_\tau u_\tau)$ with respect to k^{sgs}/u_τ^2.

the PDF for cases B0 and B1 nearly collapse; however, at $z^+ = 450$ and 550, the PDF in Case B1 is broader compared to Case B0. In particular, the standard deviation of $\lambda_3^{sgs}/(\rho_\tau u_\tau)$ at $z^+ = 450$ and 550 increases by 100% and 200%, respectively, due to stratification. Such a behavior can be attributed to the presence of internal waves (see Figs. 2 and 3) and enhanced density fluctuations caused by the formation of the pycnocline.

Apart from affecting the resolved and the SGS quantities, the stratification also affects the time evolution of quantities such as Re_τ and Nu, which are used to assess the approach to a statistically stationary state. Figure 8 shows the evolution of these quantities. Note that all the stratified cases are started after the neutral cases attain a statistically stationary state. Therefore, in Case B1, initially, Re_τ reduces sharply by approximately 15%, which can be considered as an approach towards laminarization. However, this transient behavior occurs due to competing effects of buoyancy and the shear-generated turbulence. After the sharp initial decay of Re_τ, the mean flow accelerates and a transition to fully developed turbulence state occurs. Such behavior of Re_τ has also been observed in past studies [11,13]. Overall, it takes about $12t^*$ for the Case B1 to again reach the same level of Re_τ as in Case B0, where $t^* = (t - t_0)u_\tau/h$, with t_0 being the time at which Case B1 is initialized from Case B0. The transition time is affected by the employed numerical method and the SGS model (discussed later in Sec. IV D). The value of Nu reduces in Case B1 during the statistically stationary state due to a decrease in the wall-normal gradient of the density field with an increase of Ri_τ. However, the transitional phase is evident in the time evolution of Nu.

The instantaneous flow features shown here qualitatively demonstrate the ability of the dynamic one-equation-based SGS model to capture the key features associated with stable stratification in a manner similar to those reported in the past studies [11,13]. Next, the capabilities of the model are examined in terms of the turbulence statistics.

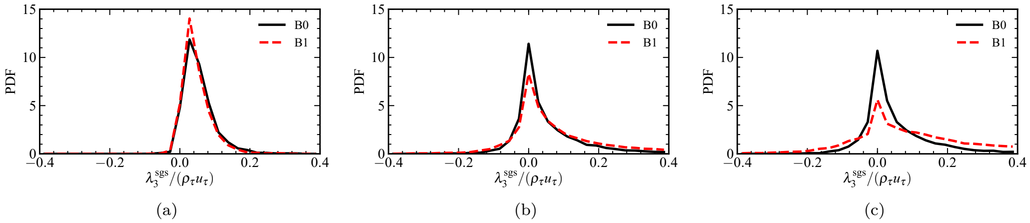

FIG. 7. PDF of the normalized SGS density flux $[\lambda_3^{sgs}/(\rho_\tau u_\tau)]$ at fixed value of the normalized SGS turbulent kinetic energy (k^{sgs}/u_τ^2) for the neutral (Case B0) and the stratified (Case B1) cases. The PDF is obtained at $k^{sgs}/u_\tau^2 = 1.0 \pm 0.02$ for (a) $z^+ = 10$, and at $k^{sgs} = 0.2 \pm 0.02$ for (b) and (c) $z^+ = 450$ and 550.

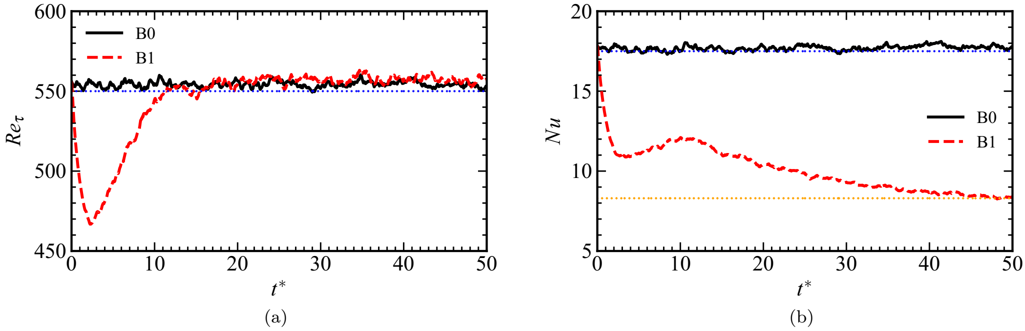

(a) (b)

FIG. 8. Time evolution of Re_τ (a) and Nu (b) for the neutral (Case B0) and the stratified (Case B1) cases. Here $t^* = (t - t_0)u_\tau/h$ is the nondimensional time, with t_0 denoting an arbitrary time instant at which Case B0 exhibits a statistically stationary state of turbulence. The dotted line in panel (a) corresponds to $\mathrm{Re}_\tau = 550$, and in panel (b) they correspond to $\mathrm{Nu} = 17.5$ and $\mathrm{Nu} = 8.3$ for cases B0 and B1, respectively.

B. Resolved turbulence statistics

The effects of stratification on the vertical variation of the first- and second-order resolved turbulence statistics are shown in Figs. 9, 10, and 11, where results obtained from cases B0 and B1 are compared with the reference DNS [13] results. The first-order statistics include the normalized mean velocity ($\langle\overline{u}\rangle/u_\tau$) and the normalized mean density ($(\langle\overline{\rho}\rangle + \Delta\rho/2)/\Delta\rho$). The second-order statistics include the streamwise intensity (u_{rms}), vertical intensity (w_{rms}), spanwise intensity (v_{rms}), intensity of the density fluctuations (ρ_{rms}), and the vertical turbulent momentum flux ($\langle u'w'\rangle$) and the buoyancy flux ($\langle w'\rho'\rangle$).

The first-order statistics compared with the reference DNS results in Fig. 9 show that Case B1 captures the effect of stable stratification. As the flow in the channel is driven by a constant pressure gradient, a constant value of u_τ (or τ_{w}) is attained (see Table I and Fig. 8). Although the vertical profile of $\langle\overline{u}\rangle$ exhibits the same behavior in the near-wall region, the stratification effect shows up in the region farther away from the wall, which increases the bulk velocity U_{b}. This manifests into an overall decrease in the skin friction coefficient C_{f} according to Eq. (12), which is a key feature of this flow [9,11,13,22]. The mean density profile shows a thicker boundary layer in Case B1 due to a reduced value of $(d\langle\overline{\rho}\rangle/dz)|_{\mathrm{w}}$, which manifests into a decrease of Nu as per Eq. (12). However, near the center of the channel, $d\langle\overline{\rho}\rangle/dz$ increases sharply in Case B1, which is due to formation of a pycnocline [2]. In comparison to DNS, LES under predicts the value of the normalized mean

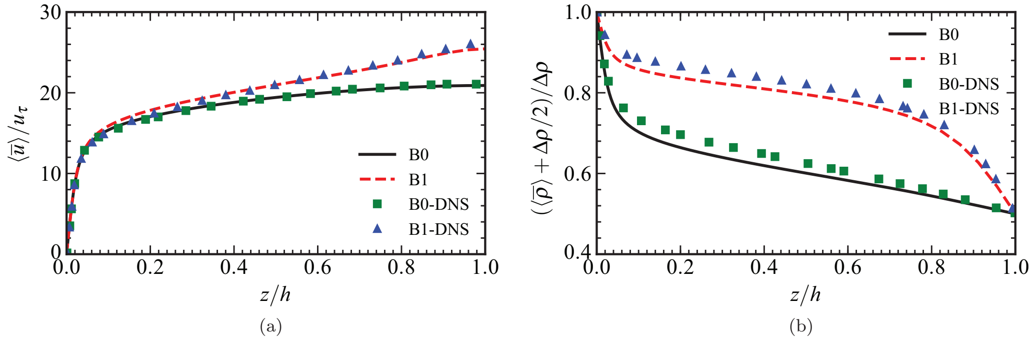

(a) (b)

FIG. 9. Profile of the normalized mean streamwise velocity (a) and density along the vertical direction compared with the reference DNS [13] results.

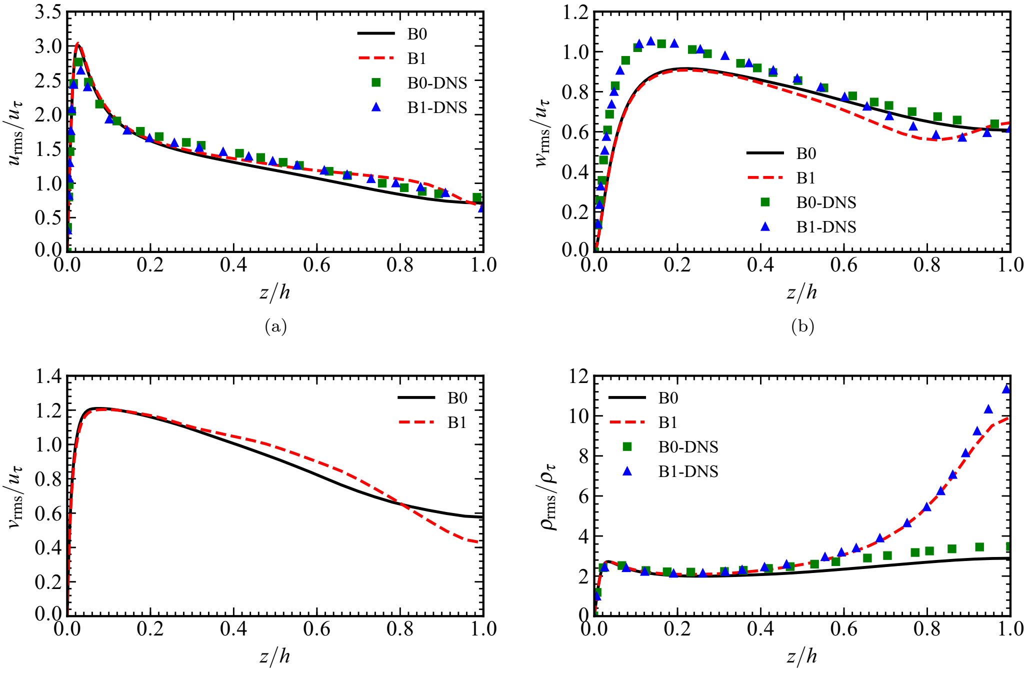

(a) (b) (c) (d)

FIG. 10. Profile of the normalized turbulence intensity of the streamwise (a), vertical (b), and spanwise (c) velocity components, and the density fluctuations (d) along the vertical direction compared with the reference DNS [13] results. Note that reference DNS results for $v_{\rm rms}$ are not available and, therefore, are not included in panel (c).

density in the region away from the wall ($0.1 < z/h < 0.4$), with a maximum error of about 6% in both cases.

Further quantification of the effects of stratification on the turbulence statistics is summarized for all cases in Table I in terms of the prediction of $C_{\rm f}$ and Nu. The stable stratification leads to a decrease in $C_{\rm f}$ and Nu by about 18% and 54%, respectively, in Case B1 compared to Case B0. These results pertaining to the effects of stratification on these quantities in wall-bounded turbulent channel flow are consistent with the past DNS study [13]. Quantitatively, the baseline LES (Case

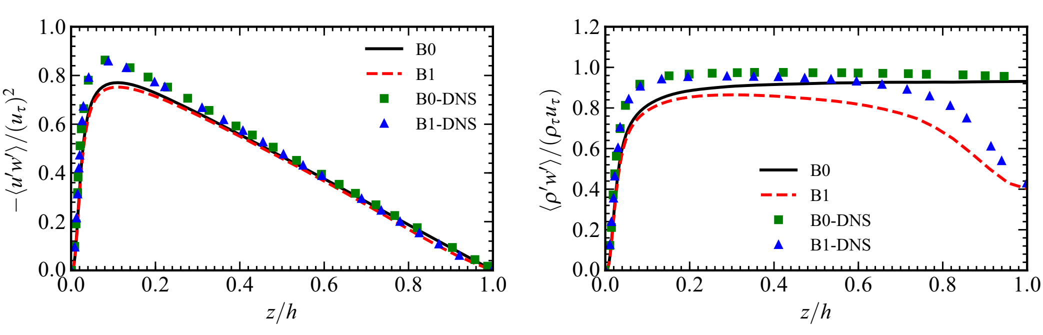

(a) (b)

FIG. 11. Profile of the mean normalized vertical turbulent momentum flux (a) and the buoyancy flux (b) along the vertical direction compared with the reference DNS [13] results.

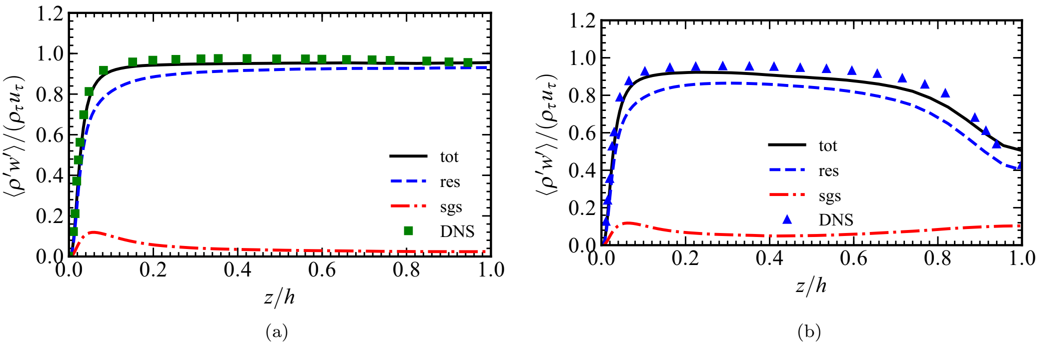

FIG. 12. Profile of the mean normalized vertical turbulent buoyancy flux (total, resolved, and SGS) for the neutral (a) (Case B0) and the stratified (b) (Case B1) compared with the reference DNS [13] results.

B0 and Case B1) predictions of C_f are within 1% for both the cases compared to the DNS results. However, the values of Nu are overpredicted in the LES cases by about 6% and 15% for Case B0 and Case B1, respectively, which can be attributed to the overprediction of $(d\langle\overline{\rho}\rangle/dz)|_\mathrm{w}$ at the wall as observed in Fig. 9(b).

The turbulence intensities of the velocity and the density fluctuations are shown in Fig. 10. Stratification affects the variation of u_rms marginally in the near-wall region, but the effects are apparent in the core and towards the center of the channel ($0.4 \leqslant z/h \leqslant 0.9$). Both cases B0 and B1 underpredict the vertical intensity (w_rms) in the near-wall region compared to the DNS results due to a significant contribution by the corresponding SGS terms (discussed below). Away from the wall, profiles from LES cases approach the DNS results. In particular, the suppression of vertical mixing in Case B1 leads to lower values of w_rms for $0.4 \leqslant z/h \leqslant 0.9$ compared to Case B0 as part of the kinetic energy gets converted to potential energy. However, near the center of the channel, the value of w_rms sharply increases due to enhanced fluctuations in the vertical component of the velocity resulting from the presence of internal waves, which leads to vertical velocity and density fluctuations [13]. This nonmonotonic variation in the stratified case in regions away from the wall is accurately captured by Case B1, which implies that the dynamic one-equation-based SGS model can respond appropriately to the effects of stratification on the turbulence dynamics. The spanwise intensity v_rms shows only a minor effect of the stratification in the near-wall region, but shows noticeable effects farther away from the wall, where the variation of the intensity of the density fluctuations also gets affected due to stratification [see Fig. 10(d)]. Such a behavior is associated with the presence of internal waves in the core region and the formation of pycnocline near the center of the channel.

The vertical variation of the vertical component of the turbulent momentum flux ($\langle u'w'\rangle$) and the buoyancy flux ($\langle w'\rho'\rangle$) (resolved quantities) compared with the reference DNS results are shown in Fig. 11. The stable stratification affects the variation of $\langle w'\rho'\rangle$ much more compared to the variation of $\langle u'w'\rangle$ consistent to the past experimental study [65]. In Case B0, $\langle w'\rho'\rangle$ saturates to a constant value ($\approx$1) away from the wall, which corresponds to the "constant flux" hypothesis of the neutral boundary layers [9]. However, in Case B1, the value of $\langle w'\rho'\rangle$ shows a significant deviation from an $O(1)$ quantity, and its value is consistently lower compared to Case B0 throughout the channel. In comparison to the reference DNS case, $\langle w'\rho'\rangle$ is underpredicted, particularly in the near-wall region. This can be attributed to a comparison of the resolved statistics from LES with the total (resolved and SGS) statistics from DNS as the magnitude of the SGS turbulence statistics is significant in such regions. This is evident from Fig. 12, where the profiles of the resolved, SGS and total buoyancy flux are shown along the vertical direction for the neutral (Case B0) and stratified (Case B1) cases. Here the total buoyancy flux is approximately defined as the sum of the resolved buoyancy flux ($\langle w'\rho'\rangle$) and the SGS buoyancy flux (λ_3^sgs) through: $\langle w'\rho'\rangle_\mathrm{tot} \approx \langle w'\rho'\rangle + \langle\lambda_3^\mathrm{sgs}\rangle$. It is apparent from

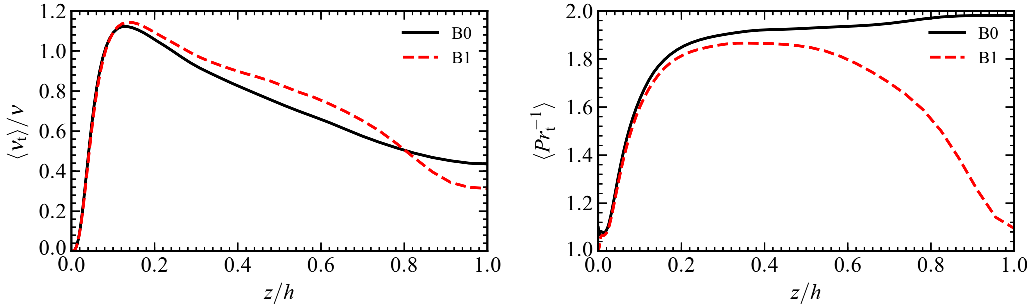

(a)

(b)

FIG. 13. Profile of the mean normalized eddy viscosity (a), the inverse of turbulent Prandtl number (b) along the vertical direction.

Fig. 12 that the agreement of the total buoyancy flux improves with the corresponding DNS results. It also illustrates that the SGS flux contributes significantly in comparison to the resolved flux. For example, in the near-wall region, the contribution by the SGS flux at its peak location is about 14% in both the neutral (Case B0) and the stratified (Case B1) cases. At the center of the channel, the contribution of the SGS buoyancy flux increases to about 20% in the stratified case.

C. SGS turbulence statistics

The variation of the SGS quantities $\langle \nu_t \rangle / \nu$ and $\langle \mathrm{Pr}_t^{-1} \rangle$ is shown in Fig. 13. Similar to the resolved second-order statistics shown in Figs. 10 and 11, the near-wall behavior of $\langle \nu_t \rangle / \nu$ and $\langle \mathrm{Pr}_t^{-1} \rangle$ is similar in Case B0 and Case B1. Stratification primarily affects the variation of these quantities for $z/h \gtrapprox 0.1$, where turbulent transport and internal waves tend to coexist. Similar to the variation of u_{rms} and v_{rms}, $\langle \nu_t \rangle / \nu$ in the stratified case is higher in the core of the channel ($0.15 \leqslant z/h \leqslant 0.8$). Since ν_t depends upon C_ν and k^{sgs}, and as discussed below that C_ν varies in the same manner in both the cases in this region of the channel, therefore, the increase in $\langle \nu_t \rangle / \nu$ occurs due to an increase in k^{sgs}. The value of $\langle \nu_t \rangle$ significantly reduces for $z/h > 0.8$ in Case B1 compared to Case B0, which can be attributed to the conversion of the kinetic energy to potential energy due to stratification. In both cases, the contribution of SGS closure is significant as $\langle \nu_t \rangle$ is about 30%–120% of the laminar kinematic viscosity (ν) throughout the channel.

The value of $\langle \mathrm{Pr}_t^{-1} \rangle$ increases away from the wall before saturating to a value of about 1.8 in the core region of the channel in both the cases. Particularly, in Case B1, $\langle \mathrm{Pr}_t^{-1} \rangle$ is lower compared to Case B0 throughout the channel and shows a sharp decrease towards the center of the channel in a manner similar to the variation of $\langle w'\rho' \rangle$ as shown in Fig. 11(b). This is expected, as due to stratification, the total buoyancy flux, $w'\rho'$, is suppressed in most parts of the channel, thus reducing even its SGS component, λ_3^{sgs}. As $\langle \mathrm{Pr}_t^{-1} \rangle > 1$ in both the cases, therefore, the magnitude of λ_3^{sgs} is finite, which implies that the magnitude of the resolved vertical buoyancy flux $\langle w'\rho' \rangle$ is lower compared to DNS as evident in Fig. 11(b). Furthermore, Fig. 13(b) also shows that although $\langle \mathrm{Pr}_t^{-1} \rangle$ is an $O(1)$ quantity, it shows a significant vertical variation [also shown before in Fig. 5(b)], and therefore, specifying an arbitrary static value may not be adequate while conducting LES. Such a significant variation of $\langle \mathrm{Pr}_t^{-1} \rangle$ from an $O(1)$ quantity has also been reported in the past DNS study [13].

The vertical variation of the model coefficients C_ν and C_ϵ, are shown in Fig. 14 for both cases. A significant variation of these coefficients occurs along the vertical direction, thus illustrating the need to model them dynamically. Similar to the variation of $\langle \nu_t \rangle$ and $\langle \mathrm{Pr}_t^{-1} \rangle$ shown in Fig. 13, stratification affects these coefficients significantly in the outer region, particularly for $0.6 \leqslant z/h \leqslant 1$. Due to suppression of turbulent mixing in the vertical direction, $\langle C_\nu \rangle$ shows a significant decrease in its value, however, a nonmonotonic variation occurs, where a sudden increase occurs towards the center

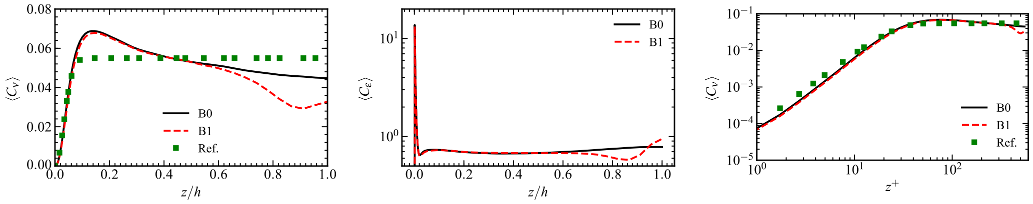

(a)

(b)

(c)

FIG. 14. Profile of the mean model coefficients $\langle C_\nu \rangle$ (a), (c) and $\langle C_\epsilon \rangle$ (b) along the vertical direction. The variation of $\langle C_\nu \rangle$ in inner coordinates is shown in panel (c). The symbols (🟩) in panels (a) and (c) correspond to the reference analytical expression given by Eq. (13).

of the channel. Such a variation of $\langle C_\nu \rangle$ is similar to the variation of w_{rms} as shown in Fig. 10(b). The nonmonotonic variation of C_ϵ is also present in the stratified case for $0.6 \leqslant z/h \leqslant 1$, thus implying that the SGS quantities respond to the dynamics associated with stratified wall-bounded turbulent flows.

The near-wall behavior of $\langle C_\nu \rangle$ shown in Fig. 14(c) in terms of the inner coordinates does not exhibit the effects of stratification, which is consistent to the other resolved and SGS turbulence statistics shown in Figs. 10, 11, and 13. While $\langle C_\nu \rangle$ increases monotonically and saturates to a quasiconstant value farther away from the wall, $\langle C_\epsilon \rangle$ (not shown here) shows a peak value in the near-wall region at the location corresponding to the peak of turbulence intensity ($z^+ \approx 10$) and then decays farther away from the wall. In particular, $\langle C_\nu \rangle$ compares very well with the behavior in the near-wall region given by

$$\langle C_\nu \rangle = 0.055[1 - e^{-(z^+/A^+)^m}]^n, \tag{13}$$

where A^+ is the damping constant, and m and n are parameters. Similar to the past study [46], A^+, m and n are specified to be 25, 2, and 1, respectively. Such exponential damping functions with different values of m and n have also been reported in the other studies of wall-bounded turbulent flows [66,67]. The effect of stratification on these model coefficients is primarily evident in regions away from the wall where both the model coefficients exhibit a nonmonotonic variation, thus demonstrating the response of the SGS model to the stratification. However, with a further increase in the level of stratification (not considered in this study), Eq. (13), may need further modifications by including Ri_g as a parameter to characterize the effects of stratification in the near-wall region.

D. Sensitivity to SGS models

Now the results obtained with three different types of SGS closures are compared for both the neutral and the stratified cases. Apart from the dynamic one-equation-based SGS model, the other two models include the “no-model” (NM) and the “dynamic Smagorinsky” (DSM) [34] approaches. The NM approach neglects all the SGS terms, which can be considered as an implicit LES approach where the required SGS dissipation is provided by the employed numerical method [68]. The DSM approach is considered here as it is the most widely used SGS closure model for different types of turbulent flows. The conventional DSM model proposed by Germano *et al.* [34] is used here with no further modifications to explicitly account for the effects of stratification. It has also been used to investigate stratified turbulent flows with a relatively finer grid resolution compared to that used for corresponding neutral turbulent flows [33]. All the model coefficients in the cases employing DSM are computed dynamically including the Pr_t used for computing the SGS density flux following the approaches described in Germano *et al.* [34] and Moin *et al.* [52]. In the following, only a limited comparison is performed to show similarities and differences in the prediction of instantaneous

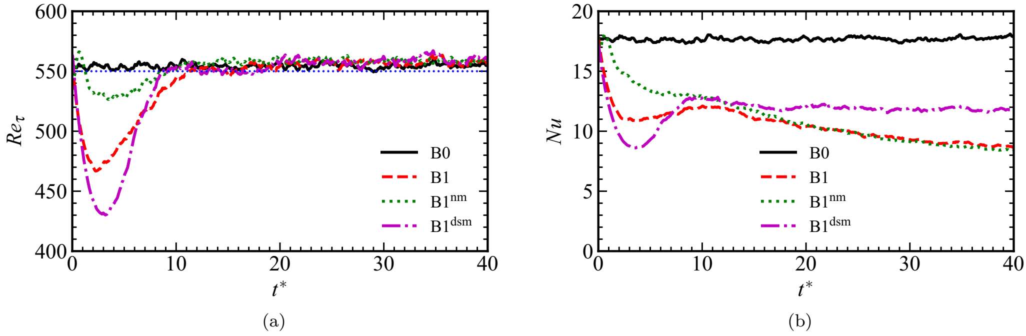

(a)

(b)

FIG. 15. Time evolution of Re_τ (a) and Nu (b) obtained from cases employing different SGS modeling approaches. The baseline cases B0 and B1 correspond to neutral and stratified conditions, respectively. The cases $\mathrm{B1^{nm}}$ and $\mathrm{B1^{dsm}}$ employ the no-model and the dynamic Smagorinsky approach, respectively, for the SGS closure and correspond to stratified condition. The dotted line in panel (a) corresponds to $\mathrm{Re}_\tau = 550$.

and statistical quantities by different modeling approaches. A detailed comparison of different SGS modeling approaches for stratified turbulent flows is out of scope of the present study.

A major difference between different models is seen in the time evolution of Re_τ and Nu in Fig. 15. Since all the stratified cases are initialized from their corresponding neutral cases, there is an initial sharp decay in the value of Re_τ due to the laminarization process (also discussed in Sec. IV A). Such a physical behavior has been reported in the past studies [9,11,13]. However, compared to the cases employing the DSM and the dynamic one-equation model, the NM stratified case shows an initially unphysical increase in Re_τ and Nu, which occurs due to lack of SGS dissipation in the NM approach. This illustrates that the NM approach can be problematic for temporally evolving cases. After an initial decay, Re_τ approaches the target value of 550 in all the cases, although the minimum attained and the subsequent rate of increase, differs in the different cases as the amount of SGS dissipation is not the same. The role of SGS dissipation is further evident in this transitional phase to the statistically stationary state, again demonstrating that an unphysical temporal evolution can occur in the NM cases. Similar to Re_τ, the time evolution of Nu exhibits a sharp initial decay followed by a transitional phase to reach the statistically stationary state. However, the approach to such a state by Nu again differs among the three SGS modeling strategies. Similar to temporal evolution of Re_τ, the initially unphysical temporal evolution is evident in the NM case compared to the other cases that have explicit SGS dissipation.

The first-order statistics of the mean streamwise velocity (not shown here) matches the reference DNS results for both the neutral and the stratified cases. However, the density field obtained in LES exhibits noticeable differences, particularly under the stratified conditions as shown in Figs. 16(a) and 16(b). The DSM approach shows substantial differences from the reference results and the predictions by the other models. There is an overprediction of Nu by about 47% as well (see Table I). It would appear that the effect of stratification is not captured, both in the near-wall and the central regions of the channel. The inability of the DSM approach to account for the effects of stable stratification is further evident from the underprediction of the density fluctuations near the center of the channel as shown in Figs. 16(c) and 16(d). An improvement in prediction using DSM has been reported using a relatively finer grid [33], but was not pursued further. The NM and the baseline one-equation model approaches agree with the DNS results. Although the time- and spatially averaged (along the x and y directions) profiles of the first-order statistics from the NM approach agree with the baseline LES and the reference DNS results, such an approach is dependent upon the employed numerical method as there is no explicit modeling of the unresolved turbulent diffusion, which affects the temporal evolution of the flow and the density fields as observed in Fig. 15.

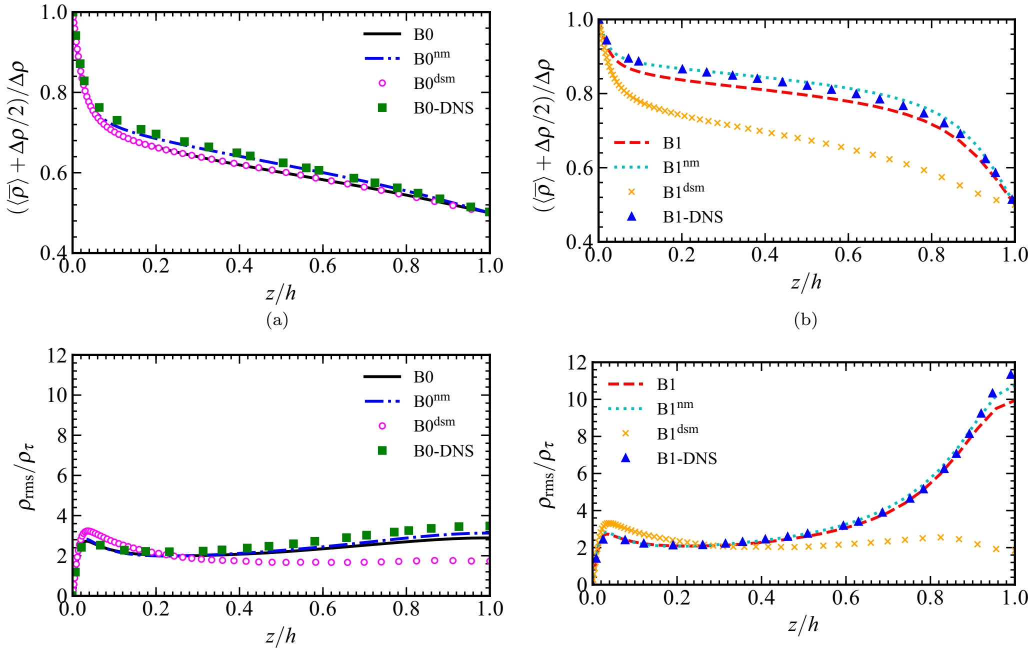

(a)

(b)

(c)

(d)

FIG. 16. Vertical variation of $(\langle\rho\rangle + \Delta\rho/2)/\Delta\rho$ (a), (b) and $\rho_{\rm rms}/\Delta\rho$ (c), (d) obtained from LES cases employing different modeling strategies and compared with the reference DNS [13] cases for neutral (a), (c) and stratified (b), (d) conditions. The cases B0 and B1 correspond to the baseline LES cases under neutral and stratified conditions, respectively. The cases labeled with superscripts "nm" and "dsm" correspond to LES cases employing the no-model and the dynamic Smagorinsky approach, respectively.

V. LES PREDICTIONS OF HIGH Re_τ AND Ri_τ EFFECTS

In this section, the dynamic one-equation-based SGS model is used to simulate cases for a range of Re_τ and Ri_τ to assess its predictive capabilities. Specifically, to examine the effects of increase in Re_τ, results from three values of $\mathrm{Re}_\tau = 180$, 550, and 950 are considered for neutral ($\mathrm{Ri}_\tau = 0$) and stratified ($\mathrm{Ri}_\tau = 60$) conditions. While DNS results for stratified turbulent channel flow are available for $\mathrm{Re}_\tau = 180$ and 550 [13], there is no such study at $\mathrm{Re}_\tau = 950$. Additionally, to assess the effects of an increase in the level of stratification, results from progressively increasing values of $\mathrm{Ri}_\tau = 0$, 60, 120, and 240 are considered at a fixed $\mathrm{Re}_\tau = 550$.

A. Effects of increase in Reynolds number

The effects of an increase in Re_τ under neutral and stratified conditions on the first- and second-order resolved turbulence statistics and the statistics of the SGS quantities are shown in Fig. 17. The mean streamwise velocity and the density fields show a collapse in the near-wall region under both neutral and stratified conditions for all values of Re_τ considered here. The effects of an increase in Re_τ are observed primarily in the outer region, i.e., core and towards the center of the channel. Under the stratified condition, as Ri_τ is increased, the stable stratification leads to a quasiparabolic profile of the mean streamwise velocity field and a sharp gradient of the density field near the center of the channel. With an increase in Re_τ, the effect of stratification is gradually pushed farther away from the wall, which is evident from both the first- and second-order statistics shown here. This is due to the dominance of the effects of shear generated turbulence over the buoyancy effect as Re_τ is increased.

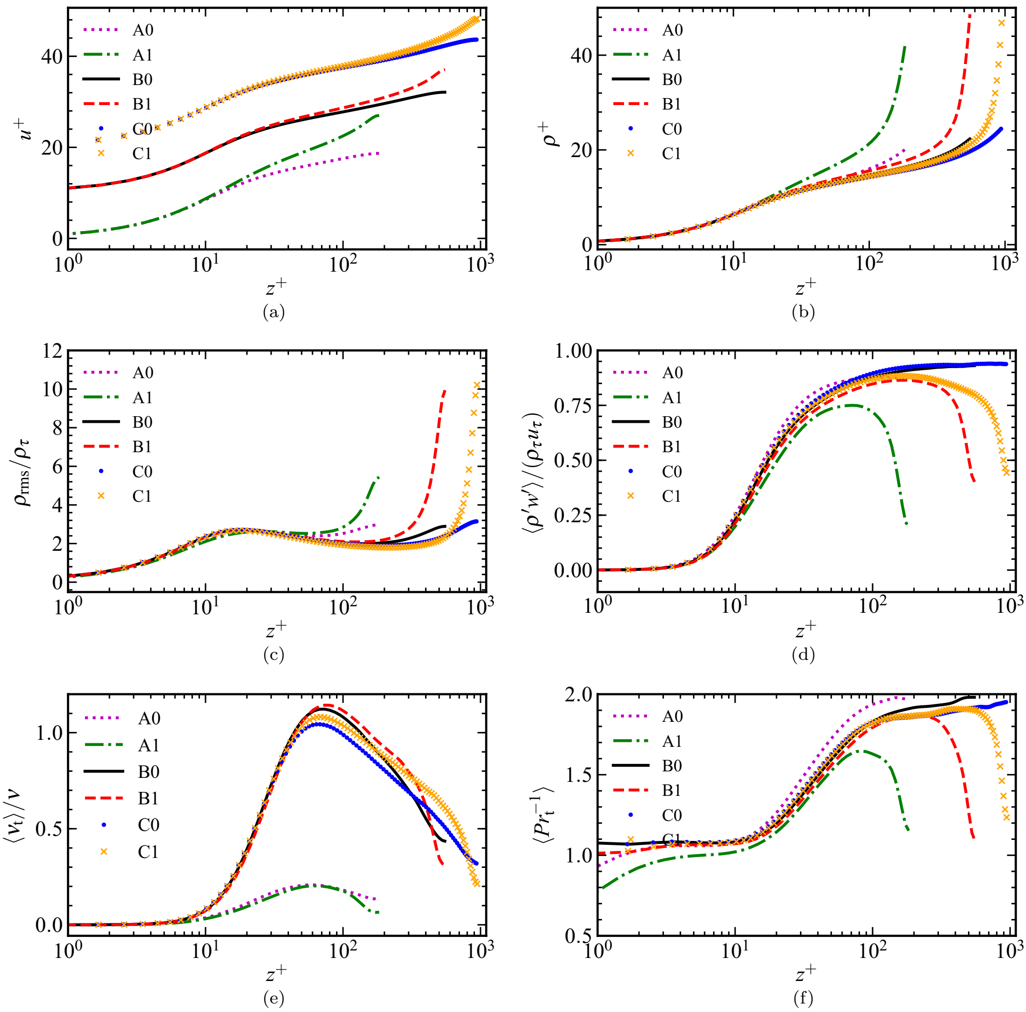

FIG. 17. Profile of u^+ (a), ρ^+ (b), $\rho_{\rm rms}$ (c), $\langle\rho'w'\rangle/\rho_\tau u_\tau$ (d), $\langle\nu_t\rangle/\nu$ (e) and $\langle \mathrm{Pr}_t^{-1}\rangle$ along the vertical direction in inner coordinates for different Reynolds number under neutral (A0, B0, C0) and stratified (A1, B1, C1) conditions. The cases A0/A1, B0/B1, and C0/C1, correspond to $\mathrm{Re}_\tau = 180$, 550, and 950, respectively.

Although, qualitatively the behavior of both first- and second-order statistics under neutral and stratified conditions remains similar at all Re_τ, these quantities show a strong dependence on Re_τ, as also evident from values of $C_{\rm f}$ and Nu reported in Table I. In particular, the decrease in $C_{\rm f}$ due to stratification reduces from about 40% to 16% as Re_τ is increased from 180 to 950. However, Nu decreases due to stratification by approximately 50% for all values of Re_τ.

Similar to the resolved statistics, the statistics of the SGS quantities shown in Fig. 17 further highlights the role of SGS closure particularly for the higher Re_τ cases. For example, the peak value of ν_t is about 20% of ν in $\mathrm{Re}_\tau = 180$ case, whereas it becomes comparable to or higher than ν in the other two higher Re_τ cases. This is also related to the employed grid in these cases where, in the $\mathrm{Re}_\tau = 180$ case, the employed grid resolution is relatively finer compared to the other two cases as apparent from the simulation parameters summarized in Table I. The dynamic model responds appropriately to the effects of stratification in all the cases where the major effects are observed in the core region and towards the center of the channel. The profile of $\langle \mathrm{Pr}_t^{-1}\rangle$ again illustrates its

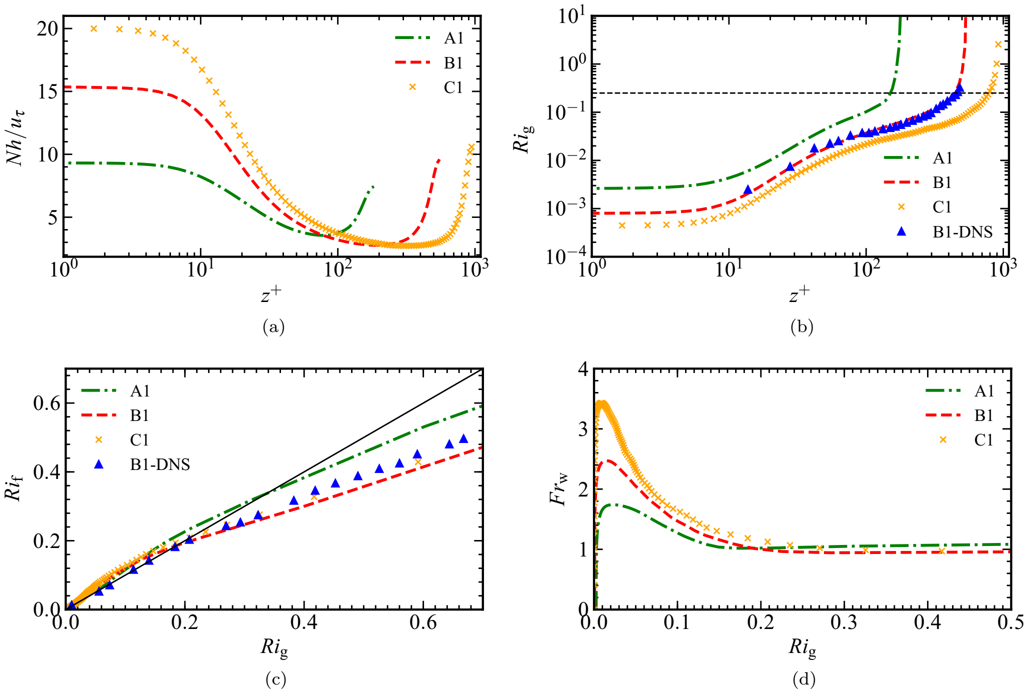

(a)

(b)

(c)

(d)

FIG. 18. Profile of normalized buoyancy frequency (Nh/u_τ) (a), and the gradient Richardson number $\mathrm{Ri_g}$ (b) along the vertical direction in inner coordinates, and the variation of flux Richardson number ($\mathrm{Ri_f}$) (c), and the vertical Froude number ($\mathrm{Fr_w}$) (d) with respect to $\mathrm{Ri_g}$ for different Reynolds number under stratified conditions. The cases A1, B1, and C1, correspond to $\mathrm{Re}_\tau = 180$, 550, and 950, respectively. The dashed curve in panel (b) corresponds to $\mathrm{Ri_g} = 0.25$.

deviation from a constant value, thus demonstrating the need to compute it in a locally dynamic manner.

The effect of increase in Re_τ on several quantities relevant to stratified flows, such as the buoyancy frequency (N), the gradient Richardson number ($\mathrm{Ri_g}$), the flux Richardson number ($\mathrm{Ri_f} = \frac{g\langle\rho' w'\rangle}{\rho_0\langle u'w'\rangle\frac{\partial\langle\overline{u}\rangle}{\partial z}}$), and the vertical Froude number ($\mathrm{Fr_w} = w_{\mathrm{rms}}/NL_e$) are shown in Fig. 18. Here L_e denotes the Ellison scale. By definition, $N = 0$ for neutral flows and it characterizes the frequency of oscillation of a fluid particle due to stratification. $\mathrm{Ri_g}$ has been extensively used in past studies [5,14,60] of the uniformed shear flow with linear stratification to analyze the effects of stratification on turbulence. These studies have shown that for $\mathrm{Ri_g} \approx 0.25$, turbulence neither decays or grows, whereas for lower values of $\mathrm{Ri_g}$ turbulence grows, and for higher values of $\mathrm{Ri_g}$ turbulence attenuates. While $\mathrm{Ri_f}$ is typically used to represent mixing efficiency, $\mathrm{Fr_w}$ represents the importance of vertical buoyancy force in comparison to the vertical momentum.

It is apparent from Fig. 18(a) that N varies along the vertical direction in all the stratified cases for all values of Re_τ. The value of N decreases sharply in the near-wall region, followed by a region of nearly constant values in all the cases before an abrupt increase occurs towards the center of the channel. The vertical extent of the region where N stays nearly constant increases with an increase in Re_τ, which is expected for a fixed value of Ri_τ. The effect of stratification is felt near the center of the channel in all the cases, which is also evident from the variation of $\mathrm{Ri_g}$ shown in Fig. 18(b), where an abrupt increase in the slope occurs above $\mathrm{Ri_g} \approx 0.2$. The profile of $\mathrm{Ri_g}$ at $\mathrm{Re}_\tau = 550$ obtained from LES agrees with the profile obtained from the reference DNS [13] results.

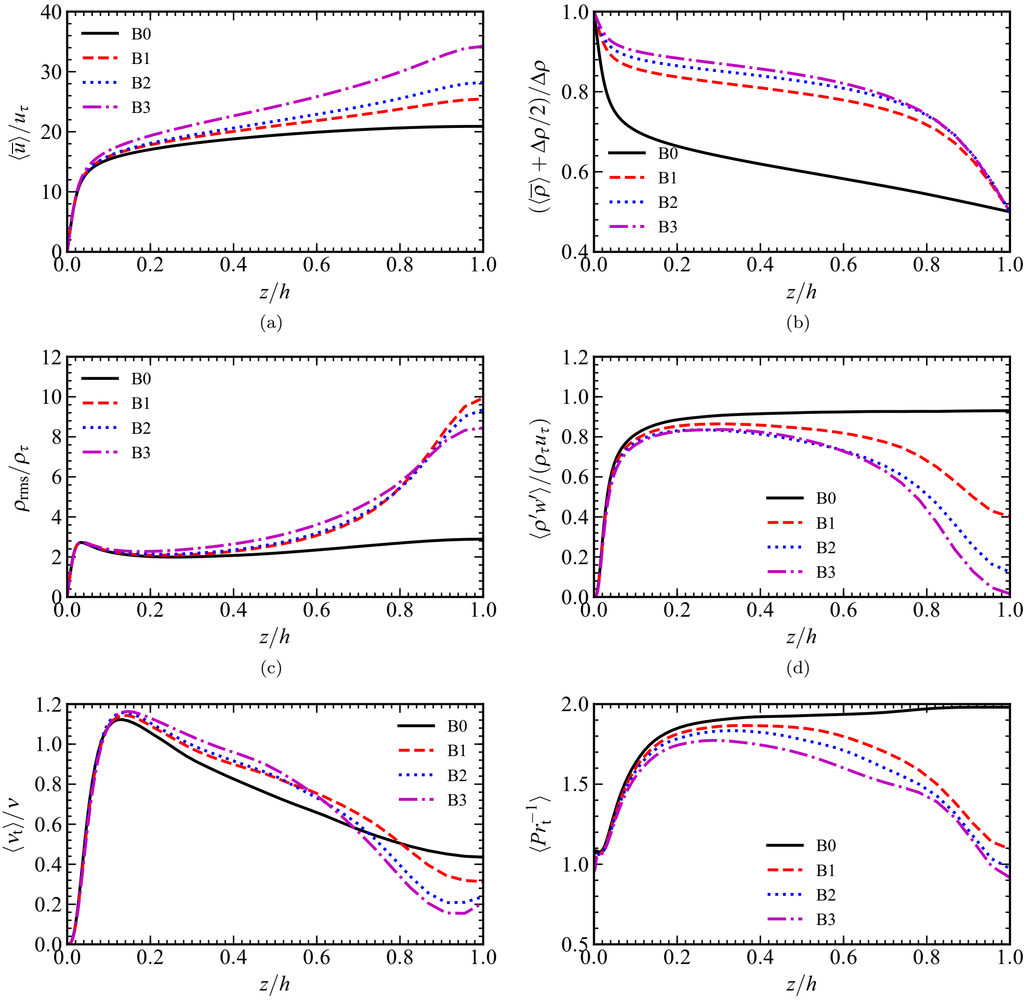

(a)

(b)

(c)

(d)

(e)

(f)

FIG. 19. Profile of $\langle\overline{u}\rangle/u_\tau$ (a), $(\langle\overline{\rho}\rangle+\Delta\rho/2)/\Delta\rho$ (b), $\rho_{\mathrm{rms}}/\rho_\tau$ (c), $\langle\rho'w'\rangle/\rho_\tau u_\tau$ (d), $\langle\nu_t\rangle$ (e), and $\langle\mathrm{Pr}_t^{-1}\rangle$ (f) along the vertical direction obtained from LES cases at $\mathrm{Re}_\tau = 550$ for different values of Ri_τ. Cases B0, B1, B2, and B3 correspond to $\mathrm{Ri}_\tau = 0$, 60, 120, and 240, respectively.

The variation of Ri_f, which represents mixing efficiency, is monotonically increasing with Ri_g [see Fig. 18(c)] in all cases. The profiles for all cases nearly collapse to the line representing $\mathrm{Ri}_\mathrm{f} = \mathrm{Ri}_\mathrm{g}$ for $\mathrm{Ri}_\mathrm{g} < 0.2$, which implies that Ri_g can be used to characterize the flow at these values of Re_τ, however, beyond $\mathrm{Ri}_\mathrm{g} > 0.2$, the profiles show significant deviations, similar to the findings of the past studies [9,13]. In all cases, Fr_w decreases monotonically for $\mathrm{Ri}_\mathrm{g} < 0.2$, which implies that the vertical buoyancy force becomes increasingly important in the vertical momentum balance. As expected, with an increase in Re_τ, the peak value of Fr_w increases. In all cases Fr_w asymptotes to $O(1)$ constant for large values of Ri_g, which agrees with the observation of a past study [69].

B. Effects of Richardson number

The ability of the dynamic one-equation-based SGS model to capture the effects of an increase in the level of stratification consistently is shown in Fig. 19. Here cases with $\mathrm{Ri}_\tau = 0$, 60, 120,

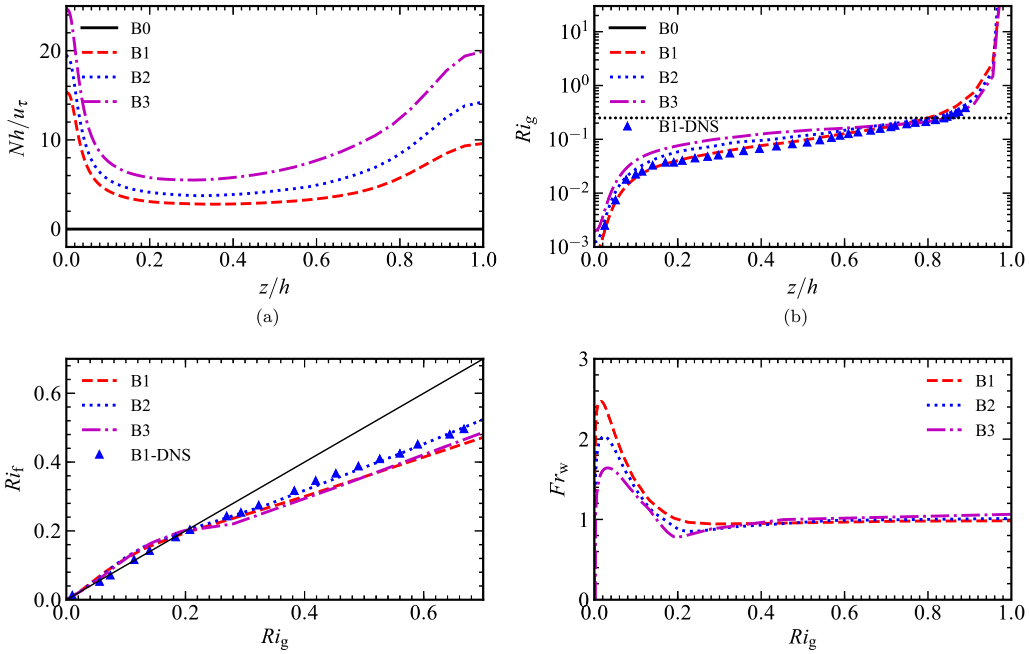

(a) (b)

(c) (d)

FIG. 20. Profile of Nh/u_τ (a) and $\mathrm{Ri_g}$ (b) along the vertical direction, and the variation of $\mathrm{Ri_f}$ (c), and $\mathrm{Fr_w}$ (d) with respect to $\mathrm{Ri_g}$ from LES cases at $\mathrm{Re}_\tau = 550$ for different values of Ri_τ. Case B0 correspond to neutral condition and cases B1, B2, and B3 correspond to $\mathrm{Ri}_\tau = 60$, 120, and 240, respectively. Case B1-DNS denotes reference DNS case at $\mathrm{Re}_\tau = 550$ and $\mathrm{Ri}_\tau = 60$.

and 240 are considered for a fixed $\mathrm{Re}_\tau = 550$. The first-order statistics of the mean streamwise velocity and the density fields shown in Figs. 19(a) and 19(b), respectively, clearly demonstrate a consistent trend with an increase in Ri_τ. In particular, the bulk velocity increases with an approach to a parabolic profile near the center of the channel, which is evident from a decrease of C_f shown in Table I by about 40% with an increase in Ri_τ from 0 to 240. The density field shows the effects of stratification throughout the channel. In particular, in the near-wall region, the vertical gradient of density gradually reduces with an increase in Ri_τ, which is also evident from the values of Nu shown in Table I where Nu reduces by about 70% with an increase in Ri_τ from 0 to 240. Additionally, the formation of a pycnocline occurs near the center of the channel in all the stratified cases, where the vertical gradient of density increases with an increase in Ri_τ.

The second-order statistics of the density fluctuation also show a consistent behavior in Fig. 19(c) with an increase in Ri_τ. The near-wall region does not show much effect of the stratification, however, the effect is evident for $z/h \gtrapprox 0.3$. The major effect is observed near the center of the channel, which is also the case with the transport of the density fluctuation as shown in Fig. 19(d), where $\langle \rho' w' \rangle$ approaches zero near the center of the channel. Note that a negative value of $\langle \rho' w' \rangle$ implies the presence of countergradient transport, which has been observed in past studies of stratified flows [5,9]. However, for the levels of stratification considered here such type of turbulent transport is not evident. The effects of an increase in Ri_τ on the SGS quantities is also evident from Figs. 19(e) and 19(f) where vertical variation of $\langle \nu_t \rangle$ and $\langle \mathrm{Pr}_t^{-1} \rangle$ are shown. The overall shape of the profile along the vertical direction for these quantities stays the same, although the values differ and the effect is gradual as Ri_τ is increased. The response of the SGS model in the core and towards the center of the channel is evident from the variation of both these quantities and demonstrates a direct

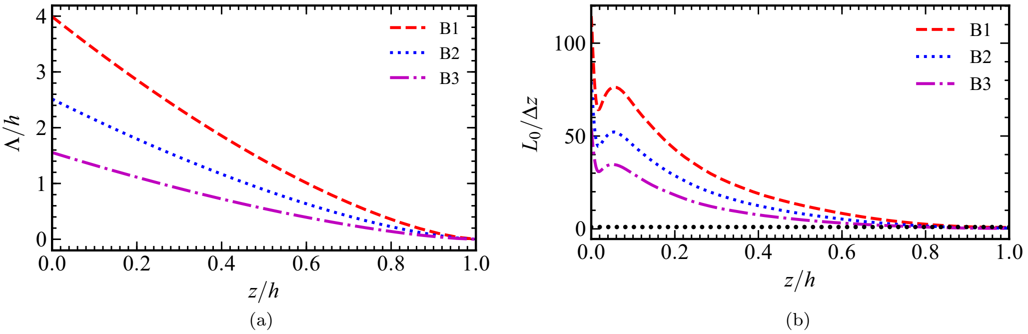

FIG. 21. Profile of Λ/h (a) and $L_0/\Delta z$ (b) along the vertical direction obtained from the stratified cases at $\mathrm{Re}_\tau = 550$ for different values of Ri_τ. Cases B1, B2, and B3 correspond to $\mathrm{Ri}_\tau = 60$, 120, and 240, respectively. The reference horizontal dotted curve in panel (b) corresponds to $L_0/\Delta z = 1$.

response of the model to the competing effects of shear-generated turbulence and buoyancy, which affects the resolved as well as the SGS turbulence dynamics in this particular flow configuration.

The effects of an increase of Ri_τ on several quantities relevant to stratified turbulent flows are shown in Fig. 20. It can be observed that N decreases sharply near the wall, stays nearly constant in the core region, and increases rapidly in a narrow region close to the center of the channel. This occurs due to the presence of internal waves as discussed before and the formation of pycnocline in the stratified cases. Such a variation of N along the vertical direction in wall-bounded flows is well established [9,70]. Ri_g remains below 0.1 in the near-wall region and most parts of the channel [see Fig. 20(b)], implying sustained turbulence in the near-wall region. However, towards the center of the channel, $\mathrm{Ri}_\mathrm{g} > 0.25$ is also observed implying attenuation of turbulence and the effects of internal waves. For all values of Ri_τ considered here, Ri_f increases monotonically with Ri_g and the profiles nearly collapse for $\mathrm{Ri}_\mathrm{g} < 0.2$ [see Fig. 20(c)], which is similar to that observed in past studies [9,13]. However, the profiles of Ri_f tend to deviate for $\mathrm{Ri}_\mathrm{g} > 0.2$. The profiles of Fr_w decreases continuously with increase in Ri_g for $\mathrm{Ri}_\mathrm{g} < 0.2$ and for larger values of Ri_g, Fr_w approaches an $O(1)$ constant, similar to that reported in the past studies [9,69].

The increase in Ri_τ affects the flow structures as evident in Fig. 2 and therefore, this effect is now examined in terms of the well-established length scales, such as the Obukhov scale, and the Ozmidov scale, which are shown in Fig. 21. Similar to the past studies [13,71], a local Obukhov scale $\Lambda(z) = -\rho_0 \tau_\mathrm{w}^{3/2}(1 - z/h)^{3/2}/\kappa g Q_\mathrm{w}$ is considered, which is the length scale at which local turbulent energy production balances the local buoyancy flux. Here κ is the Kármán constant and $\Lambda(0)$ is the Obukhov length scale, which can also be used as a length scale to parametrize the level of stratification. In the stratified cases considered here, $\Lambda(z)$ decreases along the vertical direction and also reduces throughout the channel with the increase in the level of stratification. These results further show that the turbulent structures, particularly in the outer region, get affected due to stratification. The Ozmidov scale $L_0 = \sqrt{\epsilon/N^3}$, where ϵ is total turbulent dissipation, is an estimate of the size of the largest possible eddy that can overturn in the presence of stratification. Figure 21(b) shows the variation of $L_0/\Delta z$ in a manner similar to the past studies [9,33], where Δz is the vertical grid spacing. It can be observed that $L_0/\Delta z > 1$ in most parts of the channel and $L_0/\Delta z \approx 1$ only in a very narrow region near the center of the channel in all the stratified cases, implying that all the cases resolve up to the Ozmidov scale throughout the channel.

VI. CONCLUSIONS

The locally dynamic one-equation-based subgrid-scale (SGS) model for large-eddy simulation (LES) of turbulent flows has been extended in this study to account for the effects of density stratification under the Boussinesq approximation. The SGS formulation utilizes a modeled transport equation for the SGS turbulent kinetic energy (k^{sgs}), which in turn is used to obtain the eddy viscosity. The extension of the model to stratified flows leads to an explicit coupling of k^{sgs} with the SGS density flux. For the closure of the SGS density flux, an algebraic eddy diffusivity-based approach is used. All the model coefficients used by the SGS model developed here are obtained locally and dynamically in space and time, respectively, by using the notion of test filtering and scale similarity.

The dynamic SGS model is comprehensively assessed for its predictive capabilities by considering a fully developed turbulent flow in a periodic channel with stable stratification for a range of Reynolds ($\mathrm{Re}_\tau = 180,\ 500$, and 950) and Richardson ($\mathrm{Ri}_\tau = 0$, 60, 120, and 240) numbers. First, the instantaneous and statistical features of the neutral ($\mathrm{Ri}_\tau = 0$) and the stratified ($\mathrm{Ri}_\tau = 60$) cases are examined for a fixed $\mathrm{Re}_\tau = 550$. The analysis of results showed that the dynamic SGS model is able to capture all the key features of this particular flow configuration due to stable stratification, such as suppression of turbulent transport along the vertical direction, increase in the bulk velocity, decrease of the skin friction coefficient and Nusselt number, a suppression of the mean density gradient in the near-wall region of the channel, and a sharpening of the mean density gradient (formation of pycnocline) near the center of the channel. The investigation of results also illustrated the dynamics of turbulence associated with the competing effects of shear-generated turbulence and internal waves due to stratification, which has also been reported in past studies. Furthermore, the statistical results for the resolved quantities under neutral and stratified conditions showed behavior similar to as observed in the reference direct numerical simulation (DNS) results. The analysis of the statistics of the SGS quantities demonstrated that the dynamic SGS model appropriately responds to the modifications to the flow and the density fields induced by the presence of stable stratification.

The SGS model is further assessed by comparing the statistical results with those obtained from a static approach to specify the turbulent Prandtl number (Pr_t), the use of different types of algebraic SGS models such as the "no-model" and the "dynamic Smagorinsky" approaches, and the use of a relatively finer computational grid. Overall, the results obtained from the dynamic SGS model performs well compared to the other approaches. In particular, a significant vertical variation of statistics of Pr_t^{-1} illustrated the need to specify it locally and dynamically instead of prescribing it as an arbitrary constant value. The comparison with other well-established approaches showed the role of explicitly accounting for the effects of stratification on the SGS quantities, which affects the resolved statistics. Although the "no-model" approach captured the effects of stratification on the statistical quantities, it showed an unphysical behavior in the temporal evolution of Re_τ and Nu, particularly during the initial and the transient phase to the statistically stationary state. These results showed that such an approach relies on the diffusion provided by the employed numerical method, which can incur numerical instabilities under different flow conditions compared to the use of an explicit physics-based SGS model.

Finally, the model is examined for its predictive capabilities by examining the results for $\mathrm{Re}_\tau =$ 180, 550, and 950 under neutral ($\mathrm{Ri}_\tau = 0$) and stratified ($\mathrm{Ri}_\tau = 60$) conditions, and a progressively increasing value of $\mathrm{Ri}_\tau = 0$, 60, 120, and 240 for a fixed $\mathrm{Re}_\tau = 550$. Overall, the dynamic one-equation SGS model consistently captured the effects of both an increase in Re_τ and Ri_τ, thus demonstrating that the SGS quantities appropriately respond to the modifications in the turbulence dynamics induced by stable stratification. Although the SGS model developed here captured key instantaneous flow features and turbulence statistics, the formation of a pycnocline near the center of the channel due to stratification for all values of Re_τ can lead to the presence of countergradient turbulent transport, particularly under higher levels of stratification. This in turn can potentially lead to a backscatter of SGS turbulent kinetic energy. The future studies will focus on including this aspect of SGS turbulence physics as the dynamic SGS model developed in this study assumes a co-gradient turbulent transport, and a forward cascade of the SGS kinetic energy is also implied. Additionally, other application studies such as stratified turbulent wake flows will be considered in the future to further demonstrate the predictive capabilities of the model.

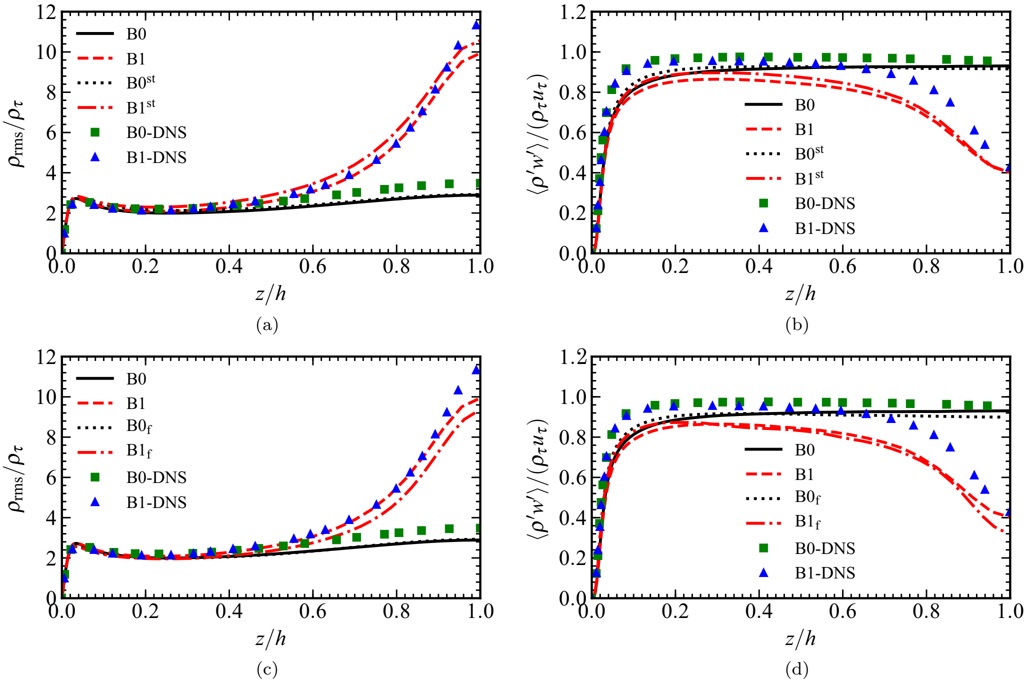

(a) (b) (c) (d)

FIG. 22. Profile of $\rho_{\mathrm{rms}}/\rho_\tau$ (a), (c), and $\langle \rho' w' \rangle / \rho_\tau u_\tau$ (b), (d), along the vertical direction obtained from LES cases and compared with the reference DNS [13] results. Cases B0 and B1 denote the baseline LES cases under neutral and stratified conditions, respectively, employing fully dynamic approach, whereas cases B0$^{\mathrm{st}}$ and B1$^{\mathrm{st}}$ denote the neutral and stratified cases, respectively, employing the static approach to specify Pr_t. Cases B0$_{\mathrm{f}}$ and B1$_{\mathrm{f}}$ use a relatively finer grid resolution.

ACKNOWLEDGMENTS

This work was supported by the Office of Naval Research (ONR) under Grant No. N00014-16-1-2577. The computation time provided by the DOD HPC center at Navy DSRC is highly appreciated.

APPENDIX: SENSITIVITY TO APPROACHES FOR SPECIFYING Pr_t AND GRID RESOLUTION

In this Appendix the sensitivity of the statistics to the approaches employed for specification of Pr_t and to the employed grid are discussed. It is well established to use a dynamic approach to compute all the model coefficients while conducting LES [34,35,46]. Typically, the model coefficients can vary locally in space and time as already shown in Secs. IV A and IV C. To assess the effects of the way the coefficients are specified or computed to obtain the SGS scalar flux (λ_j^{sgs}) on the prediction of the turbulence statistics, two types of cases, labeled as Case B0$^{\mathrm{st}}$ and Case B1$^{\mathrm{st}}$ are considered for the neutral and the stratified conditions, respectively. For the static cases, a nominal value of $\mathrm{Pr}_t = 1$ is used, whereas, for the dynamic cases, Pr_t varies in both space and time depending upon the local flow condition. However, in both the static and the dynamic cases, the eddy viscosity ν_t is still obtained dynamically using the LDKM approach [46]. The adequacy of the baseline grid employed in this study is illustrated by considering a relatively finer grid. Past LES studies of stratified turbulent channel flow [9,11] employed a much finer grid resolution than that typically used for LES of wall-bounded turbulent channel flows. Therefore, a relatively finer grid resolution is considered here, which approximately matches the coarsest grid resolution used in the past studies.

The variation of the first-order statistics do not show differences between the static and dynamic cases, and between the baseline and the relatively fine grid cases. Therefore, these statistics are not shown here for brevity. The differences are primarily observed in the second-order statistics, some of which are shown in Fig. 22. With regard to use of static and dynamic way to specify Pr_t, a noticeable effect is evident in the variation of $\rho_{\mathrm{rms}}/\rho_\tau$ and $\langle\rho' w'\rangle/\rho_\tau u_\tau$ [see Figs. 22(a) and 22(b)], where both of these quantities are predicted to be of higher magnitude in the static cases. This can be attributed to a reduced level of dissipation of the scalar field fluctuations compared to the dynamic cases where $\langle \mathrm{Pr}_t^{-1}\rangle \geqslant 1$ throughout the channel [see Fig. 13(b)]. The profile of $\langle \nu_t\rangle$ (not shown here) does not show the effect of static versus dynamic formulation as it is computed dynamically in both the cases.

The effects of grid resolution are also evident on the variation of the second-order statistics [see Figs. 22(c) and 22(d)]. In particular, the near-wall variation of ρ_{rms} from the baseline and the fine grid cases show a collapse with the DNS results, but the differences are apparent in the outer region, where LES cases tend to underpredict the intensity compared to the DNS results under both neutral and stratified conditions. Similar to the baseline grid, the fine grid case can capture the effect of stratification on the behavior of turbulent buoyancy flux $\langle\rho' w'\rangle$. Overall, the fine grid results only show a minor improvement in the prediction of $\langle\rho' w'\rangle$ in comparison to the baseline grid case.

The effects of stratification on the global quantities C_{f}, and Nu for these cases are also summarized in Table I. Overall, both the static and dynamic cases correctly capture the effects of stratification. In particular, C_{f} and Nu decreases by about 17% and 56%, respectively, in the stratified case with respect to the values of the neutral case. The predicted values of these global quantities by the static cases are within 2%–3% of the values corresponding to the dynamic cases. The cases employing different grid resolutions can capture the effects of stratification in a manner consistent with the reference DNS results. In particular, compared to the baseline grid LES case where C_{f} and Nu decreases by 18% and 54%, respectively, due to stratification, these quantities respectively decrease by 17% and 52% in the fine grid case. These results further illustrate that the baseline grid, which is about 30% of the relatively fine grid, is adequate for an LES-based investigation for conditions considered in the present study.

---

[1] J. S. Turner, *Buoyancy Effects in Fluids* (Cambridge University Press, Cambridge, 1979).
[2] H. J. S. Fernando, Turbulent mixing in stratified fluids, Annu. Rev. Fluid Mech. **23**, 455 (1991).
[3] R. Grimshaw, *Environmental Stratified Slows* (Springer Science & Business Media, New York, 2002), Vol. 3.
[4] J. R. Herring and O. Métais, Numerical experiments in forced stably stratified turbulence, J. Fluid Mech. **202**, 97 (1989).
[5] S. E. Holt, J. R. Koseff, and J. H. Ferziger, A numerical study of the evolution and structure of homogeneous stably stratified sheared turbulence, J. Fluid Mech. **237**, 499 (1992).
[6] T. Gerz and H. Yamazaki, Direct numerical simulation of buoyancy-driven turbulence in stably stratified fluid, J. Fluid Mech. **249**, 415 (1993).
[7] E. C. Itsweire, J. R. Koseff, D. A. Briggs, and J. H. Ferziger, Turbulence in stratified shear flows: Implications for interpreting shear-induced mixing in the ocean, J. Phys. Oceanogr. **23**, 1508 (1993).
[8] V. M. Canuto and F. Minotti, Stratified turbulence in the atmosphere and oceans: A new subgrid model, J. Atmos. Sci. **50**, 1925 (1993).
[9] V. Armenio and S. Sarkar, An investigation of stably stratified turbulent channel flow using large-eddy simulation, J. Fluid Mech. **459**, 1 (2002).
[10] D. Chung and G. Matheou, Large-eddy simulation of stratified turbulence. Part I: A vortex-based subgrid-scale model, J. Atmos. Sci. **71**, 1863 (2014).
[11] R. P. Garg, J. H. Ferziger, S. G. Monismith, and J. R. Koseff, Stably stratified turbulent channel flows. I. Stratification regimes and turbulence suppression mechanism, Phys. Fluids **12**, 2569 (2000).

[12] K. A. Brucker and S. Sarkar, A comparative study of self-propelled and towed wakes in a stratified fluid, J. Fluid Mech. **652**, 373 (2010).

[13] M. Garcia-Villalba and J. C. Del Alamo, Turbulence modification by stable stratification in channel flow, Phys. Fluids **23**, 045104 (2011).

[14] J. J. Rohr, E. C. Itsweire, K. N. Helland, and C. W. Van Atta, Growth and decay of turbulence in a stably stratified shear flow, J. Fluid Mech. **195**, 77 (1988).

[15] T. Gerz, U. Schumann, and S. E. Elghobashi, Direct numerical simulation of stratified homogeneous turbulent shear flows, J. Fluid Mech. **200**, 563 (1989).

[16] L. H. Shih, J. R. Koseff, J. H. Ferziger, and C. R. Rehmann, Scaling and parameterization of stratified homogeneous turbulent shear flow, J. Fluid Mech. **412**, 1 (2000).

[17] S. K. Venayagamoorthy, J. R. Koseff, J. H. Ferziger, and L. H. Shih, Testing of RANS turbulence models for stratified flows based on DNS data, Tech. Rep., Stanford University Environmental Fluid Mechanics Lab (2003).

[18] L. H. Shih, J. R. Koseff, G. N. Ivey, and J. H. Ferziger, Parameterization of turbulent fluxes and scales using homogeneous sheared stably stratified turbulence simulations, J. Fluid Mech. **525**, 193 (2005).

[19] S. K. Venayagamoorthy and D. D. Stretch, On the turbulent Prandtl number in homogeneous stably stratified turbulence, J. Fluid Mech. **644**, 359 (2010).

[20] S. P. S. Arya, Buoyancy effects in a horizontal flat-plate boundary layer, J. Fluid Mech. **68**, 321 (1975).

[21] S. Komori, H. Ueda, F. Ogino, and T. Mizushina, Turbulence structure in stably stratified open-channel flow, J. Fluid Mech. **130**, 13 (1983).

[22] O. Iida, N. Kasagi, and Y. Nagano, Direct numerical simulation of turbulent channel flow under stable density stratification, Int. J. Heat Mass Transf. **45**, 1693 (2002).

[23] F. P. Bretherton, The propagation of groups of internal gravity waves in a shear flow, Q. J. R. Meteorol. Soc. **92**, 466 (1966).

[24] W. H. Hooke and R. M. Jones, Dissipative waves excited by gravity-wave encounters with the stably stratified planetary boundary layer, J. Atmos. Sci. **43**, 2048 (1986).

[25] B. D. Mater and S. K. Venayagamoorthy, A unifying framework for parameterizing stably stratified shear-flow turbulence, Phys. Fluids **26**, 036601 (2014).

[26] F. G. Jacobitz, S. Sarkar, and C. W. Van Atta, Direct numerical simulations of the turbulence evolution in a uniformly sheared and stably stratified flow, J. Fluid Mech. **342**, 231 (1997).

[27] J. J. Riley and S. M. DeBruynkops, Dynamics of turbulence strongly influenced by buoyancy, Phys. Fluids **15**, 2047 (2003).

[28] S. K. Venayagamoorthy and J. R. Koseff, On the flux Richardson number in stably stratified turbulence, J. Fluid Mech. **798**, R1 (2016).

[29] D. K. Lilly, On the numerical simulation of buoyant convection, Tellus **14**, 148 (1962).

[30] A. Dörnbrack, Turbulent mixing by breaking gravity waves, J. Fluid Mech. **375**, 113 (1998).

[31] J. Smagorinsky, General circulation experiments with the primitive equations, Mon. Weather Rev. **91**, 99 (1963).

[32] S. Remmler and S. Hickel, Direct and large eddy simulation of stratified turbulence, Int. J. Heat Fluid Flow **35**, 13 (2012).

[33] S. Khani and M. L. Waite, Buoyancy scale effects in large-eddy simulations of stratified turbulence, J. Fluid Mech. **754**, 75 (2014).

[34] M. Germano, U. Piomelli, P. Moin, and W. H. Cabot, A dynamic subgrid-scale eddy viscosity model, Phys. Fluids A **3**, 1760 (1991).

[35] C. Meneveau, T. S. Lund, and W. H. Cabot, A Lagrangian dynamic subgrid-scale model of turbulence, J. Fluid Mech. **319**, 353 (1996).

[36] J. Bardina, J. H. Ferziger, and W. C. Reynolds, Improved subgrid-scale models for large-eddy simulation, in *Proceedings of the AIAA 13th Fluid and Plasma Dynamics Conference, 14-16 July 1980, Snowmass, CO*, AIAA Paper 80–1357 (AIAA, Reston, VA, 1980).

[37] S. Stolz and N. A. Adams, An approximate deconvolution procedure for large-eddy simulation, Phys. Fluids **11**, 1699 (1999).

[38] J. W. Deardorff, Stratocumulus-capped mixed layers derived from a three-dimensional model, Boundary-Layer Meteorol. **18**, 495 (1980).

[39] U. Schumann, Subgrid length-scales for large-eddy simulation of stratified turbulence, Theor. Comput. Fluid Dyn. **2**, 279 (1991).

[40] B. Nebenführ and L. Davidson, Large-eddy simulation study of thermally stratified canopy flow, Boundary-Layer Meteorol. **156**, 253 (2015).

[41] U. Schumann, Subgrid scale model for finite difference simulations of turbulent flows in plane channels and annuli, J. Comput. Phys. **18**, 376 (1975).

[42] A. Misra and D. I. Pullin, A vortex-based subgrid stress model for large-eddy simulation, Phys. Fluids **9**, 2443 (1997).

[43] J. Yan, A. Korobenko, A. E. Tejada-Martínez, R. Golshan, and Y. Bazilevs, A new variational multiscale formulation for stratified incompressible turbulent flows, Comput. Fluids **158**, 150 (2017).

[44] Y. Bazilevs, V. M. Calo, J. A. Cottrell, T. J. R. Hughes, A. Reali, and G. Scovazzi, Variational multiscale residual-based turbulence modeling for large eddy simulation of incompressible flows, Comput. Methods Appl. Mech. Eng. **197**, 173 (2007).

[45] S. Menon and W. W. Kim, High Reynolds number flow simulations using the localized dynamic subgrid-scale model, in *Proceedings of the AIAA 34th Aerospace Sciences Meeting and Exhibit, 15-18 January 1996, Reno, NV,* AIAA Paper 96–0425 (AIAA, Reston, VA, 1996).

[46] W. W. Kim and S. Menon, An unsteady incompressible Navier-Stokes solver for large-eddy simulation of turbulent flows, Int. J. Numer. Methods Fluids **31**, 983 (1999).

[47] A. Yoshizawa and K. Horiuti, A statistically-derived subgrid-scale kinetic energy model for the large eddy simulation of turbulent flows, J. Phys. Soc. Jpn. **54**, 2834 (1985).

[48] S. Ghosal, T. S. Lund, P. Moin, and K. Akselvoll, A dynamic localization model for large-eddy simulation of turbulent flows, J. Fluid Mech. **286**, 229 (1995).

[49] F. Génin and S. Menon, Studies of shock/turbulent shear layer interaction using large-eddy simulation, Comput. Fluids **39**, 800 (2010).

[50] X. Chai and K. Mahesh, Dynamic-equation model for large-eddy simulation of compressible flows, J. Fluid Mech. **699**, 385 (2012).

[51] D. Brydon, S. Sun, and R. Bleck, A new approximation of the equation of state for seawater, suitable for numerical ocean models, J. Geophys. Res. [Oceans] **104**, 1537 (1999).

[52] P. Moin, K. Squires, W. Cabot, and S. Lee, A dynamic subgrid-scale model for compressible turbulence and scalar transport, Phys. Fluids A **11**, 2746 (1991).

[53] C. Y. Lee and S. Cant, Assessment of LES subgrid-scale models and investigation of hydrodynamic behaviour for an axisymmetrical bluff body flow, Flow, Turbul. Combust. **98**, 155 (2017).

[54] W. Schmidt, J. C. Niemeyer, and W. Hillebrandt, A localised subgrid scale model for fluid dynamical simulations in astrophysics—I. Theory and numerical tests, Astron. Astrophys. **450**, 265 (2006).

[55] R. Ranjan and S. Menon, A multiscale simulation method for high Reynolds number wall-bounded turbulent flows, J. Turbulence **14**, 1 (2013).

[56] R. Ranjan and S. Menon, Vorticity, backscatter and counter-gradient transport predictions using two-level simulation of turbulent flows, J. Turbulence **19**, 334 (2018).

[57] B. Vreman, B. Geurts, and H. Kuerten, On the formulation of the dynamic mixed subgrid-scale model, Phys. Fluids **6**, 4057 (1994).

[58] A. G. Gungor and S. Menon, A new two-scale model for large eddy simulation of wall-bounded flows, Prog. Aerospace Sci. **46**, 28 (2010).

[59] R. Ranjan and S. Menon, On the application of the two-level large-eddy simulation method to turbulent free-shear and wake flows, J. Turbulence **16**, 136 (2015).

[60] J. W. Miles, On the stability of heterogeneous shear flows, J. Fluid Mech. **10**, 496 (1961).

[61] A. G. Kravchenko, P. Moin, and R. Moser, Zonal embedded grids for numerical simulations of wall-bounded turbulent flows, J. Comput. Phys. **127**, 412 (1996).

[62] H. Choi and P. Moin, Grid-point requirements for large eddy simulation: Chapman's estimates revisited, Phys. Fluids **24**, 011702 (2012).

[63] F. G. Jacobitz, M. M. Rogers, and J. H. Ferziger, Waves in stably stratified turbulent flow, J. Turbulence **6**, 1 (2005).

[64] R. A. Antonia and J. Kim, Turbulent Prandtl number in the near-wall region of a turbulent channel flow, Int. J. Heat Mass Transf. **34**, 1905 (1991).

[65] C. A. G. Webster, An experimental study of turbulence in a density-stratified shear flow, J. Fluid Mech. **19**, 221 (1964).

[66] P. Moin and J. Kim, Numerical investigation of turbulent channel flow, J. Fluid Mech. **118**, 341 (1982).

[67] U. Piomelli, J. H. Ferziger, and P. Moin, Models for large eddy simulation of turbulent channel flow including transpiration, Department of Mechanical Engineering Report TF-32 (Stanford University, Stanford, California, 1987).

[68] P. R. Spalart, Strategies for turbulence modelling and simulations, Int. J. Heat Fluid Flow **21**, 252 (2000).

[69] S. Sarkar, Turbulence anisotropy in stratified uniform shear flow, in *Fifth International Symposium on Stratified Flows, Vancouver*, edited by G. A. Lawrence, R. Pieters, and N. Yonemitsu (Department of Civil Engineering, University of British Columbia, Vancouver, Canada, 2000), pp. 1245–1250.

[70] E. M. Saiki, C.-H. Moeng, and P. P. Sullivan, Large-eddy simulation of the stably stratified planetary boundary layer, Boundary-Layer Meteorol. **95**, 1 (2000).

[71] F. T. M. Nieuwstadt, The turbulent structure of the stable, nocturnal boundary layer, J. Atmos. Sci. **41**, 2202 (1984).